Phase behaviour, sedimentation and stacking in colloidal mixtures of thick and thin hard rods

Patrick Hooijer
Utrecht University
MSc. thesis

Supervisor:
Prof. Dr. René van Roij
Institute for Theoretical Physics
Utrecht University

June 30, 2015

Abstract

In this thesis we take a look at a binary mixture of thick and thin hard rods using Onsager theory, and look at their high pressure expansion to study the nematic phase more accurately. We will numerically solve the non-linear integral equations leading to the orientation distribution functions of the system for several diameter ratios, concentrations and compositions. Using these solutions, we will draw the phase diagrams summarizing the possible phases of the system, and find isotropic-nematic, nematic-nematic as well as isotropic-isotropic demixing, with corresponding isotropic-nematic-nematic and isotropic-isotropic-nematic triple points. In a few cases, a nematic-nematic or isotropic-isotropic critical point will appear.

Then we will look at sedimentation profiles by including the effects of gravity in our calculations, and calculate the paths these mixtures can take in various phase diagrams as function of the height in a test tube. Here we find many configurations of the contents of the test tube, for example an isotropic phase between two nematic phases, and the composition variable of the heavier particles that is not increasing as function of the height. We will summarize these different configurations in a phase stacking diagram, and see that this diagram is not trivial, even for the simple case where there is only isotropic-nematic phase coexistence.

1 Introduction

Colloids are particles with a typical size of 10-1000 nm, and appear in many shapes and sizes. Colloids, along with other particles like polymers and surfactants are called mesoscopic particles, because they are much heavier and larger than microscopic particles like atoms, but much lighter and smaller than macroscopic particles like desks and houses. Because of the size of colloids, they are typically classical objects instead of quantummechanical. While simultaneously having a low enough binding energy, of the order of the thermal energy, that thermal fluctuations and Brownian motion become major components in describing them. Classical statistical mechanics is usually the framework used to describe colloids.

1.1 Liquid Crystals

The gas, liquid and crystalline states of matter are well understand, and that the distinguishing feature between these states is the positional ordering of the molecules between different states. While gases and liquids do have translational and rotational symmetry, these symmetries are fully broken in the crystalline phase. This makes these phase transitions interesting to study. Since many molecules are approximately spherical, most studies involving these substances involves modelling these molecules by spheres.

For almost a century, there has been an increasing interest in other shapes as models for molecules: most commonly rod-like and disc-like colloids. The study of the phase behaviour of these kinds of molecules date back to at least the 1920s, where Zocher [1] discovered experimentally that a solution of rod-like colloids undergoes a phase transitions from an isomorphic phase to a phase where the rods are oriented along a specific direction.

Rod- and disc-like colloids exhibit additional forms of ordering compared to spherical particles: in addition to positional ordering there is also orientational ordering. The most disordered phase is the isotropic phase, where neither positions nor orientations are ordered. When all particles point in approximately the same direction, the fluid is in a nematic phase. Other phases include the smectic phase, where the particles are in addition to being ordered in one orientational direction are also ordered in one positional direction; and the crystalline phase, where the system is ordered in all three orientational and all three positional directions. Schematic configurations of these phases can be seen in Fig. 1. Because these additional phases have optical properties of a crystal, while having the mechanical properties of a liquid, these systems are called Liquid Crystals. These combinations of properties of the traditional fluid and crystalline phases makes them useful in multiple applications, for example in Liquid Crystalline Displays (LCDs).

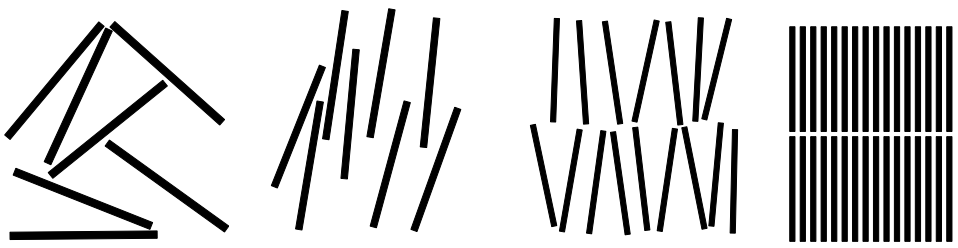

Figure 1: Typical configurations of rod-like particles in the isotropic, nematic, smectic and crystalline phases respectively. The nematic and smectic phases are examples of liquid crystal phases not appearing in a system with spherical particles; they have often the mechanical properties of a fluid, but optical properties of a crystal. This thesis focusses on the first two phases.

2 Onsager Theory for Monodisperse Systems

To study a system consisting of N colloidal particles, we have to study its Hamiltonian. In theoretical models of particles it is often assumed that the interaction between the particles is the sum over pairwise terms, each of them characterized by a pair potential $\phi(\vec{r}_i - \vec{r}_j, \vec{\Omega}_i - \vec{\Omega}_j)$ that depends on the relative coordinates of the particles $\vec{r}_i - \vec{r}_j$ and the relative orientation of the particles $\vec{\Omega}_i - \vec{\Omega}_j$. For these pairwise-additive particles, the Hamiltonian is given by [5]

$$H(\vec{p}^N, \vec{r}^N, \vec{\Omega}^N) = \sum_{i=1}^{N} \frac{\vec{p}_i^2}{2m} + \sum_{i<j}^{N} \phi(\vec{r}_i - \vec{r}_j, \vec{\Omega}_i - \vec{\Omega}_j). \tag{1}$$

In the 1940's Onsager [2] successfully explained the isotropic to nematic phase transition theoretically in terms of the interparticle interactions. He modelled rod-like particles with rigid, infinitely long rods, where the only interaction between the rods is a short-range hard-core interaction

$$\phi(\vec{r}_i - \vec{r}_j, \vec{\Omega}_i - \vec{\Omega}_j) = \begin{cases} \infty & : \text{ particle } i \text{ overlaps with particle } j \\ 0 & : \text{ otherwise} \end{cases}. \tag{2}$$

The hard-core potential does not contain any attracting force. This is present in real particles due to to Van der Waals forces, and describes the steeply repulsive interaction when two particles are very close to each other crudely. However, the hard-core potential is of great theoretical importance because it is a zeroth-order approximation in the perturbation theory of liquids. Moreover, experimental realizations of hard-core systems can be made due to advances in the synthesis of colloidal particles in the form of colloidal suspensions. Onsager used this simpel model to explain qualitatively the experimental observed interaction by Zocher [1] between the particles.

2.1 Virial Expansion

The classic ideal-gas law $\hat{p}V = Nk_BT$, where $\hat{p}$ is the pressure, V the volume, N the number of particles, k_B the Boltzmann constant and T the temperature; does not hold for real gasses at finite density $\rho = N/V$ because of the interactions between the particles. Kamerlingh-Onnes proposed the virial expansion of the pressure as correction to this law for orientational independent particles by fitting correction terms to experimental data:

$$p(\rho, T) = k_BT(\rho + B_2(T)\rho^2 + B_3(T)\rho^3 + ...) \tag{3}$$

where $B_n(T)$ are the virial coefficients. The second and third virial coefficient are respectively [5]

$$B_2(T) = -\frac{1}{2V} \int \mathrm{d}^3\vec{r}_i \int \mathrm{d}^3\vec{r}_j \big(\exp(-\beta\phi(\vec{r}_{ij})) - 1\big) = -\frac{1}{2} \int \mathrm{d}^3\vec{r} f(\vec{r}) \text{ and} \tag{4}$$

$$B_3(T) = -\frac{1}{3V} \int \mathrm{d}^3\vec{r}_i \int \mathrm{d}^3\vec{r}_j \int \mathrm{d}^3\vec{r}_k f(\vec{r}_{ij}) f(\vec{r}_{jk}) f(\vec{r}_{ki}). \tag{5}$$

Here $\vec{r}_{ij} = \vec{r}_i - \vec{r}_j$, $\beta = 1/k_BT$ is the inverse temperature and $f(\vec{r}) = \exp(-\beta\phi(\vec{r})) - 1$ is the Mayer function. We are however interested in orientational *dependent* particles and thus replace the volume element with

$$\mathrm{d}^3\vec{r} \to \frac{\mathrm{d}^3\vec{r}\,\mathrm{d}^3\vec{\Omega}}{\int \mathrm{d}^3\vec{\Omega}}. \tag{6}$$

The virial coefficients become

$$B_2(T) = -\frac{1}{2V(\int \mathrm{d}^3\vec{\Omega})^2} \int \mathrm{d}^3\vec{r} \int \mathrm{d}^3\vec{\Omega} f(\vec{r}, \vec{\Omega}), \tag{7}$$

$$\begin{aligned} B_3(T) = &-\frac{1}{3V(\int \mathrm{d}^3\vec{\Omega})^3} \int \mathrm{d}^3\vec{r}_i \int \mathrm{d}^3\vec{\Omega}_i \int \mathrm{d}^3\vec{r}_j \int \mathrm{d}^3\vec{\Omega}_j \int \mathrm{d}^3\vec{r}_k \int \mathrm{d}^3\vec{\Omega}_k \\ &\times f(\vec{r}_{ij}, \vec{\Omega}_{ij}) f(\vec{r}_{jk}, \vec{\Omega}_{jk}) f(\vec{r}_{ki}, \vec{\Omega}_{ki}), \end{aligned} \tag{8}$$

with $\vec{\Omega}_{ij} = \vec{\Omega}_i - \vec{\Omega}_j$. When filling in the hard core potential of Eq. (2), the exponential term $\exp(-\beta\phi(r_{ij}, \Omega_{ij})$ is either equal to 1 (if $\phi(r_{ij}, \Omega_{ij}) = 0$) or 0 (if $\phi(r_{ij}, \Omega_{ij}) = \infty$). This removes all dependencies on β, and thus the virial coefficients of hard-core interactions are independent on the temperature T. Thus the interactions and dynamics of the system with hard-core potentials are driven purely by the entropy of the system.

The second virial coefficient for hard rod shaped particles has been calculated by Onsager in a rather extensive calculation [2] and is equal to the excluded volume of two identical particles close to each other:

$$B_{2,\mathrm{HR}} = \frac{\pi}{2}\left(D^3|\sin\gamma| + LD^2(1 + |\cos\gamma| + E(|\sin\gamma|))\right) + 2L^2D|\sin\gamma|, \tag{9}$$

where L is the length of the rod, D is the diameter of the rod, γ is the relative angle between the rods and $E(x)$ is the elliptic integral of the second kind

$$E(x) = \int_0^{\pi/2} \mathrm{d}\varphi\sqrt{1 - x^2\sin^2\varphi}. \tag{10}$$

In the infinite needle limit, where $L \gg D$, the last term of Eq. (9) is the dominating term

$$B_{2,\mathrm{HR}}|_{L\gg D} = 2L^2D|\sin\gamma| \tag{11}$$

In the isotropic phase, where all particles are even likely to point in any direction, we can take the average of $|\sin\gamma|$, which is equal to $\langle|\sin\gamma|\rangle_{\mathrm{iso}} = 1/(\pi)\int_0^\pi \mathrm{d}\gamma|\sin\gamma| = 2/\pi$. So the second virial coefficient in the infinite needle limit in the isotropic phase is equal to

$$B_{2,\mathrm{INL,iso}} = \frac{4}{\pi}L^2D \tag{12}$$

Onsager showed that it is plausible that the third and higher virial coefficients are negligible, and subsequent numerical work supports this claim. [4]

2.2 Helmontz Free Energy

Since the dynamics of the system are driven only by entropy, the internal energy $\mathrm{d}U = T\,\mathrm{d}S - p\,\mathrm{d}V + \mu\,\mathrm{d}N$, where T is the temperature, S is the entropy, p is the pressure, V is the volume and μ is the chemical potential; is not an interesting quantity to calculate because of its independence of the entropy S. We can however perform a Legendre transformation to transform the internal energy to the Helmontz free energy $F = U - TS$, such that $\mathrm{d}F = -S\,\mathrm{d}T - p\,\mathrm{d}V + \mu\,\mathrm{d}N$. This *is* dependent on the entropy, and thus suited to study this system of infinitely long rods.

The Helmontz free energy of an ideal gas is equal to $F = Nk_BT(\log(\rho\Lambda^3) - 1)$, [5] where $\Lambda = h/\sqrt{2\pi mk_BT}$ with h Planck's constant is the thermal (De Broglie) wavelength of the particle. For interacting liquids, we can use a virial expansion similar to Eq. (3) and write

$$F(T, V, N) = Nk_BT(-1 + \log\left(\frac{N}{V}\Lambda^3\right) + B_2\frac{N}{V} + \frac{1}{3}B_3\left(\frac{N}{V}\right)^2 + \dots) \tag{13}$$

Generalizing this expression for s species of N_s particles with $N = \sum_i N_i$, Eq. (13) becomes

$$F(T, V, N_1, N_2, \dots, N_s) = k_BT(-N + \sum_{i=1}^{s} N_i\log\left(\frac{N_i}{V}\Lambda^3\right) + \frac{1}{V}\sum_{i,j=1}^{s} B_2(i,j)N_iN_j + \dots) \tag{14}$$

where $B_2(i,j) = -\frac{1}{2V}\int \mathrm{d}^3\vec{r}\int \mathrm{d}^3\vec{\Omega}\big(\exp(-\beta\phi_{ij}(\vec{r},\vec{\Omega})) - 1\big)$ is the second virial coefficient term due to interactions between particles of species i and j. When looking at a large number of particles occupying all the directions Ω, we can replace the sum with an integral

$$F(T, N, V) = k_BT(-N + \int \mathrm{d}\Omega N(\Omega)\log\left(\frac{N(\Omega)}{V}\Lambda^3\right) + \frac{1}{V}\int \mathrm{d}\Omega\int \mathrm{d}\Omega' B_2(\Omega,\Omega')N(\Omega)N(\Omega')) \tag{15}$$

where we omitted the terms of B_3 and higher order. Because rods have an axial symmetry, it is convenient to write $\mathrm{d}\Omega$ in spherical coordinates $\mathrm{d}\theta\,\mathrm{d}\varphi\sin\theta$. Next we replace $N(\Omega)$ with the

orientation distribution function (ODF) $\psi(\Omega)$, which gives the fraction of particles pointing in the Ω direction: $N(\Omega) = N\psi(\Omega)$. Filling in B_2 from Eq. (11) we arrive at

$$\begin{aligned} F(T,N,V) = Nk_BT\Big(-1 + 2\pi \log\left(\frac{N}{V}\Lambda^3\right) + 2\pi \int_0^\pi \mathrm{d}\theta \sin\theta\psi(\theta)\log(\psi(\theta)) \\ + \frac{2}{\pi}L^2 D\frac{N}{V}\int_0^\pi \mathrm{d}\theta \int_0^{2\pi}\mathrm{d}\varphi \int_0^\pi \mathrm{d}\theta' \int_0^{2\pi}\mathrm{d}\varphi' \sin\theta\sin\theta' |\sin\gamma(\theta,\varphi,\theta',\varphi')|\psi(\theta)\psi(\theta')\Big). \end{aligned} \tag{16}$$

We can write $|\sin\gamma(\theta,\theta')|$ explicitly in terms of θ and θ'

$$|\sin\gamma(\theta,\varphi,\theta',\varphi')| = \sqrt{1-(\cos\theta\cos\theta' + \sin\theta\sin\theta'\cos(\varphi-\varphi'))^2}. \tag{17}$$

Because this is the only term dependent on φ, we can move the φ integrals inside Eq. (17) and define the azimuthally averaged kernel $K(\theta,\theta')$:

$$\frac{K(\theta,\theta')}{2\pi} = \frac{1}{2\pi}\int_0^{2\pi}\mathrm{d}\varphi\int_0^{2\pi}\mathrm{d}\varphi'|\sin\gamma| = \int_0^{2\pi}\mathrm{d}\varphi\sqrt{1-(\cos\theta\cos\theta'+\sin\theta\sin\theta'\cos\varphi)^2}. \tag{18}$$

Because you can add or subtract any constant to the Helmontz free energy, we subtract the terms -1 and $\log(\Lambda^3)$. By defining the dimensionless number density $c = B_{2,\mathrm{IHR,iso}}N/V$ and the Helmontz free energy per particle per k_BT, we arrive at

$$\begin{aligned} f(c) \equiv \frac{F(T,N,V)}{Nk_BT} = \log(c) + 4\pi\int_0^{\pi/2}\mathrm{d}\theta\sin\theta\psi(\theta)\log(\psi(\theta)) \\ + 32c\int_0^{\pi/2}\mathrm{d}\theta\int_0^{\pi/2}\mathrm{d}\theta'\sin\theta\sin\theta' K(\theta,\theta')\psi(\theta)\psi(\theta'), \end{aligned} \tag{19}$$

where we used the up-down symmetry for both isotopic and nematic systems $\psi(\theta) = \psi(\pi-\theta)$. This free energy consists of an orientational entropy term f_{or}, which is part of the ideal gas term $\log c + f_{or}$, and an excess term with respect to the ideal gas due to the excluded volume of the particles f_{ex}.

One can minimize this free energy with respect to the ODF by using the Euler-Lagrange equation $\delta f/\delta\psi(\theta) = 0$, which gives

$$\lambda = \log\psi(\theta) + \frac{8c}{\pi}\int_0^\pi \mathrm{d}\theta'\sin\theta' K(\theta,\theta')\psi(\theta'), \tag{20}$$

where λ is the Lagrange multiplier that fixes the normalization $4\pi\int_0^{\pi/2}\mathrm{d}\theta\sin\theta\psi(\theta) = 1$.

This equation is a non-linear integral equation, and has not been solved analytically. It can however easily be checked that the isotropic phase $\psi_{\mathrm{iso}}(\theta) = 1/(4\pi)$ is a solution of Eq. (20) for any c. The nematic solution can be calculated using numeric methods.

Given a solution $\psi(\theta)$ of Eq. (20), we can calculate the pressure, chemical potential and order parameter of the particles

$$p \equiv \beta\hat{p}B_2 = B_2\left(\frac{\beta\partial F}{\partial V}\right)_N = \frac{\partial f}{\partial c}c^2, \tag{21}$$

$$\mu \equiv \beta\hat{\mu} = \left(\frac{\beta\partial F}{\partial N}\right)_V = f + \frac{\partial f}{\partial c}c, \tag{22}$$

$$S = 4\pi\int_0^{\pi/2}\mathrm{d}\theta\sin\theta\psi(\theta)\frac{3\cos^2\theta-1}{2}. \tag{23}$$

where p and μ are dimensionless versions of the pressure $\hat{p}$ and the chemical potential $\hat{\mu}$ respectively. Having the expression for the pressure in Eq. (21), we can perform another Legendre transformation to transform the Helmontz free energy into the Gibbs free energy: $G(T,\hat{p},N) = F + \hat{p}V$. Thus the Gibbs free energy is

$$\mathrm{d}G = \mathrm{d}F + \mathrm{d}(\hat{p}V) = -S\,\mathrm{d}T + V\,\mathrm{d}\hat{p} + \hat{\mu}\,\mathrm{d}N \tag{24}$$

$$g(p) = G/(Nk_BT) = f + \beta p B_2/c. \tag{25}$$

The Gibbs free energy is useful for studying phase equilibria, since the pressure is constant along the interface between two phases.

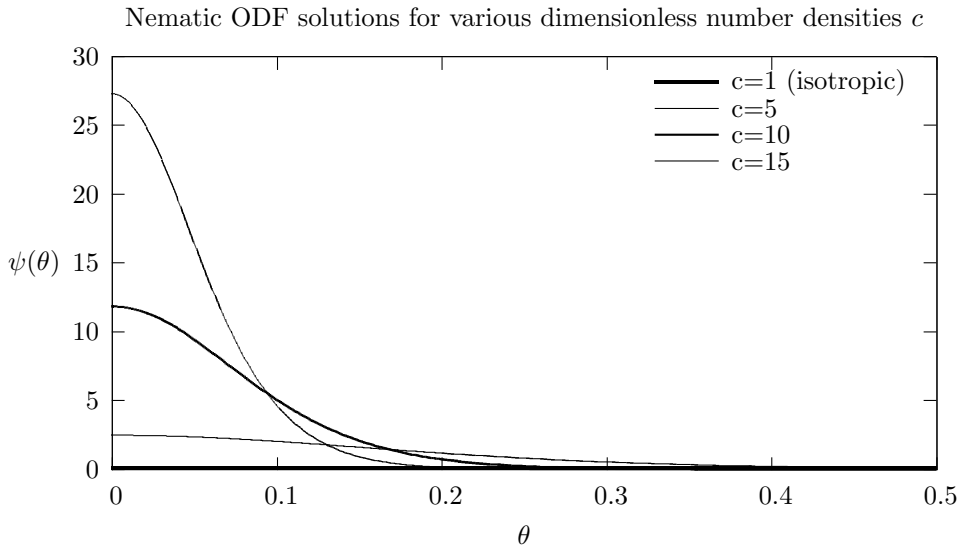

Figure 2: Nematic solutions of Eq. 20 for various dimensionless number densities c. The ODFs become more and more peaked for higher c, while having a constant surface due to the normalization. No nematic solution was found for $c = 1$, so the isotropic solution $\psi(\theta) = 1/(4\pi) \approx 0.796$ is calculated instead. The nematic solutions exponentially decay. The ODFs are only plotted for $\theta \in [0, 5]$, while the actual domain of θ is $[0, \pi/2]$.

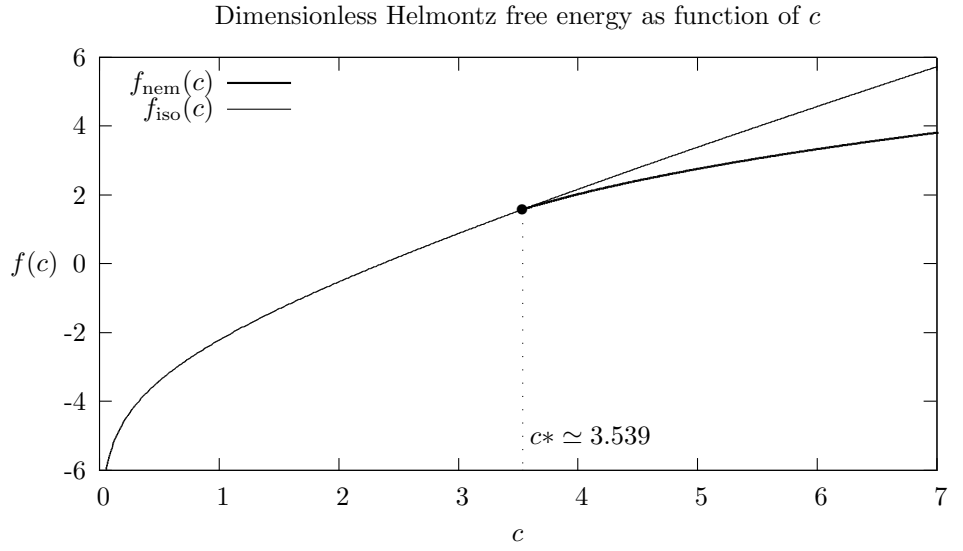

Figure 3: Dimensionless Helmontz free energy as function of the dimensionless number density. The isotropic and nematic solution have equal f for $c* \simeq 3.539$. For $c < c*$, the isotropic phase is favourable, while for $c > c*$ the nematic phase is favourable.

2.3 Numerical Methods

The non-linear integral equation of Eq. (20) can be solved using an iterative scheme, a procedure very common in the theory of many-body systems. This method is used and explained by van Roij in [6]. Starting with an initial guess $\psi_0(\theta)$, we calculate the next step $\psi_{n+1}(\theta)$ by filling in the result from the previous step $\psi_n(\theta)$ in Eq. (20):

$$\psi_{n+1}(\theta) = \frac{1}{Z} \exp\left(-\frac{8c}{\pi} \int_0^{\pi} \mathrm{d}\theta' \sin\theta' K(\theta,\theta') \psi_n(\theta') \right) \tag{26}$$

where Z is a normalization constant such that the normalization $\frac{1}{4\pi}\int_0^{\pi/2} \sin\theta \psi_{n+1}(\theta) = 1$ is satisfied. Self-consistency is obtained by applying this iterative scheme multiple times until the desired accuracy is reached.

The ODF $\psi(\theta)$ will be determined on a discrete grid of a finite set of N polar angles θ_k in the interval $[0, \pi/2]$, with $k = 1, 2, \ldots, N$. For an equidistant grid, θ_k is equal to

$$\theta_k = \frac{\pi}{2} \frac{k}{N+1}, \qquad k = 1, 2, \ldots, N, \tag{27}$$

however, other grids that are finer close to $\theta = 0$ are used , because the ODFs become very peaked for higher densities (see Fig. 2). Because $\mathrm{d}\theta \sin\theta = -\,\mathrm{d}(\cos\theta)$, we can approximate for any arbitrary function $f(\theta)$

$$\int_0^{\pi/2} \mathrm{d}\theta \sin\theta f(\theta) \approx \sum_{k=1}^{N} \Delta_k f(\theta_k), \tag{28}$$

where we define Δ_k as

$$\Delta_k \equiv \begin{cases} 1 - (\cos\theta_k + \cos\theta_{k+1})/2 & : \quad k = 1, \\ (\cos\theta_{k-1} - \cos\theta_{k+1})/2 & : \quad k = 2, 3, \ldots, N-1, \\ (\cos\theta_k + \cos\theta_{k-1})/2 & : \quad k = N. \end{cases} \tag{29}$$

This choice of Δ_k guarantees the correct normalization $\sum_{k=1}^{N} \Delta_k = 1$ for any θ-grid for $N \geq 2$. To calculate the azimuthally averaged kernel $K(\theta, \theta')$, defined in Eq. (18), a equidistant grid of the N_φ azimuthal angles φ_j with

$$\varphi_j = 2\pi \frac{j}{N_\varphi + 1}, \qquad j = 1, 2, \ldots, N_\varphi. \tag{30}$$

Using this grid, the values of $K(\theta, \theta')$ on this grid are equal to

$$K_{kl} \equiv K(\theta_k, \theta_l) = \frac{2\pi}{N_\varphi + 1} \left(\frac{3}{2} |\sin\gamma_{kl}(\varphi_1)| + \sum_{j=2}^{N_\varphi - 1} |\sin\gamma_{kl}(\varphi_j)| + \frac{3}{2} |\sin\gamma_{kl}(\varphi_{N_\varphi})| \right) \tag{31}$$

with $|\sin\gamma_{kl}(\varphi)|$ the discrete version of Eq. (17):

$$|\sin\gamma_{kl}(\varphi)| = \sqrt{1 - (\cos\theta_k \cos\theta_l + \sin\theta_k \sin\theta_l \cos\varphi)^2}. \tag{32}$$

When calculating $\psi(\theta)$ for a wide range of c_m, $m = 1, \ldots, M$, it is more efficient to use the result of the previous step as your first initial guess: $\psi_0(\theta)|_{c_m} = \psi(\theta)|_{c_{m-1}}$. Because the ODFs in Fig. 2 are very similar to the Gaussian distribution, but not identical, it is convenient to choose our first guess $\psi_0(\theta)|_{c_0} = (c_0/\pi)^2 \exp(-2c_0^2\theta^2/\pi)$. This ensures quick convergence for small enough $c_m - c_{m-1}$, except around the density where $f_{\mathrm{iso}}(c*) = f_{\mathrm{nem}}(c*)$, where the ODFs jump from a peaked function around θ to a constant function. Because Eq. (31) is independent of c, it is advised to calculate and store K_{kl} before applying the iterative scheme and load them when calculating the ODFs.

2.4 Phase separation

The dimensionless Helmontz free energy f as function of the dimensionless number density c of the isotropic and nematic phase are equal to each other at $c* \simeq 3.539$, see Fig. 3. Thus one could argue that a phase transition appears at $c = c*$, with an isotropic phase at $c < c*$ and a nematic phase at $c > c*$. However, the system can lower its energy further at a given density $c \in (c_I, c_N)$ by splitting up into a subvolume in the isotropic phase with density c_I, and a subvolume in the nematic phase with density c_N. Such a coexistence requires mechanical and diffusive equilibrium between the two phases, which are only true if the pressure and chemical potential between the two phases are the same:

$$p_{\text{iso}}(c_I) = p_{\text{nem}}(c_N) \qquad\qquad \mu_{\text{iso}}(c_I) = \mu_{\text{nem}}(c_N). \tag{33}$$

These two equations with two variables can easily be solved using numerical root finding methods. Another way of finding the two coexisting pressures c_I and c_N is by finding the common tangents of $\phi(c) \equiv f(c)c$, this is called the Maxwell construction. Finding a comment tangent of a function $\phi(c)$ is equivalent to solving

$$\left.\frac{\mathrm{d}\phi(c)}{\mathrm{d}c}\right|_{c_I} = \left.\frac{\mathrm{d}\phi(c)}{\mathrm{d}c}\right|_{c_N}, \qquad\qquad \phi(c_N) = \phi(c_I) + \left.\frac{\mathrm{d}\phi(c)}{\mathrm{d}c}\right|_{c_I}(c_N - c_I), \tag{34}$$

for variables c_I and c_N. These equations are equivalent to the equations in (33):

$$p(c) = \frac{\mathrm{d}f(c)}{\mathrm{d}c}c^2 = \frac{\mathrm{d}\phi(c)}{\mathrm{d}c}c - \phi(c) \quad \rightarrow \quad \phi(c_N) - \left.\frac{\mathrm{d}\phi(c)}{\mathrm{d}c}\right|_{c_N} c_N = \phi(c_I) - \left.\frac{\mathrm{d}\phi(c)}{\mathrm{d}c}\right|_{c_I} c_I, \tag{35}$$

$$\mu(c) = f(c) + \frac{\mathrm{d}f(c)}{\mathrm{d}c}c = \frac{\mathrm{d}\phi(c)}{\mathrm{d}c} \quad \rightarrow \quad \left.\frac{\mathrm{d}\phi(c)}{\mathrm{d}c}\right|_{c_I} = \left.\frac{\mathrm{d}\phi(c)}{\mathrm{d}c}\right|_{c_N}, \tag{36}$$

where we used Eqs. (21) and (22). This construction can be seen in Fig. 4, where the right picture is the same as the left picture minus the linear term $c\mu_{IN}$. Since $\phi(c) - c\mu(c) = \phi(c) - c\,\mathrm{d}\phi/\,\mathrm{d}c = -p(c)$, the common tangent in the right picture is a horizontal line at $-p_{IN}$.

The physical quantities at this coexistence are $c_I \simeq 3.290$, $c_N \simeq 4.191$, $\mu_{IN} \simeq 5.241$, $p_{IN} \simeq 14.12$, $S_I = 0$ and $S_N \simeq 0.7922$, where we used the definitions of Eqs. (21)-(23).

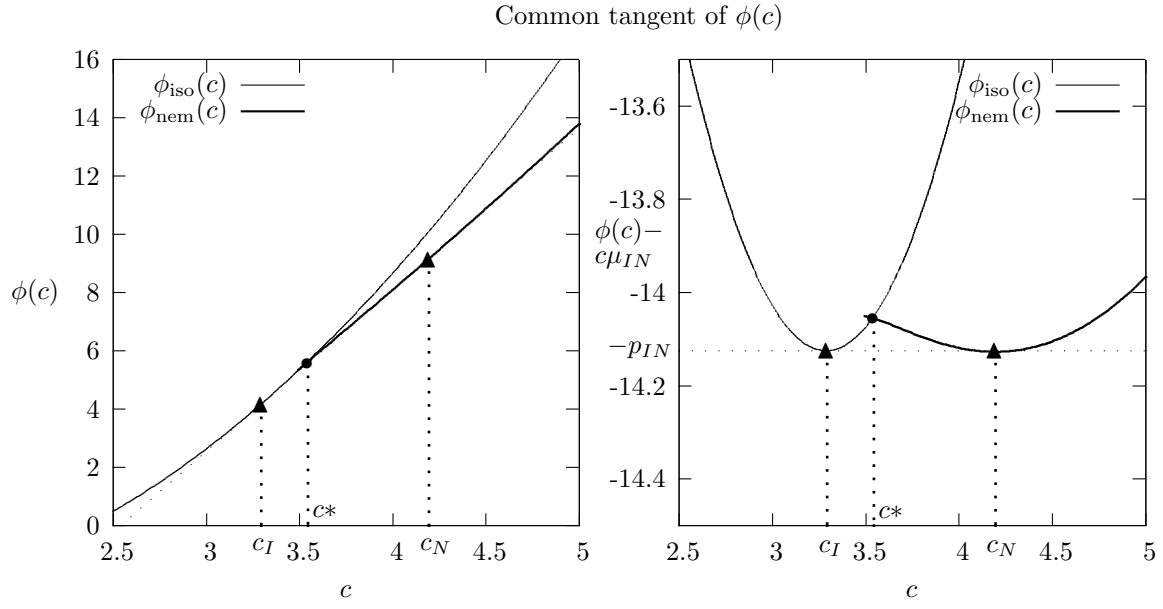

Figure 4: On the left: common tangent of $\phi(c) = cf(c)$. Because the common tangent is hard to see, we subtract in the figure right the linear term $c\mu_{IN}$, where μ_{IN} is the chemical potential at the interface. Since $\phi(c) - c\mu(c) = -p(c)$, the coexistence pressure $-p_{IN}$ can be read off the right picture.

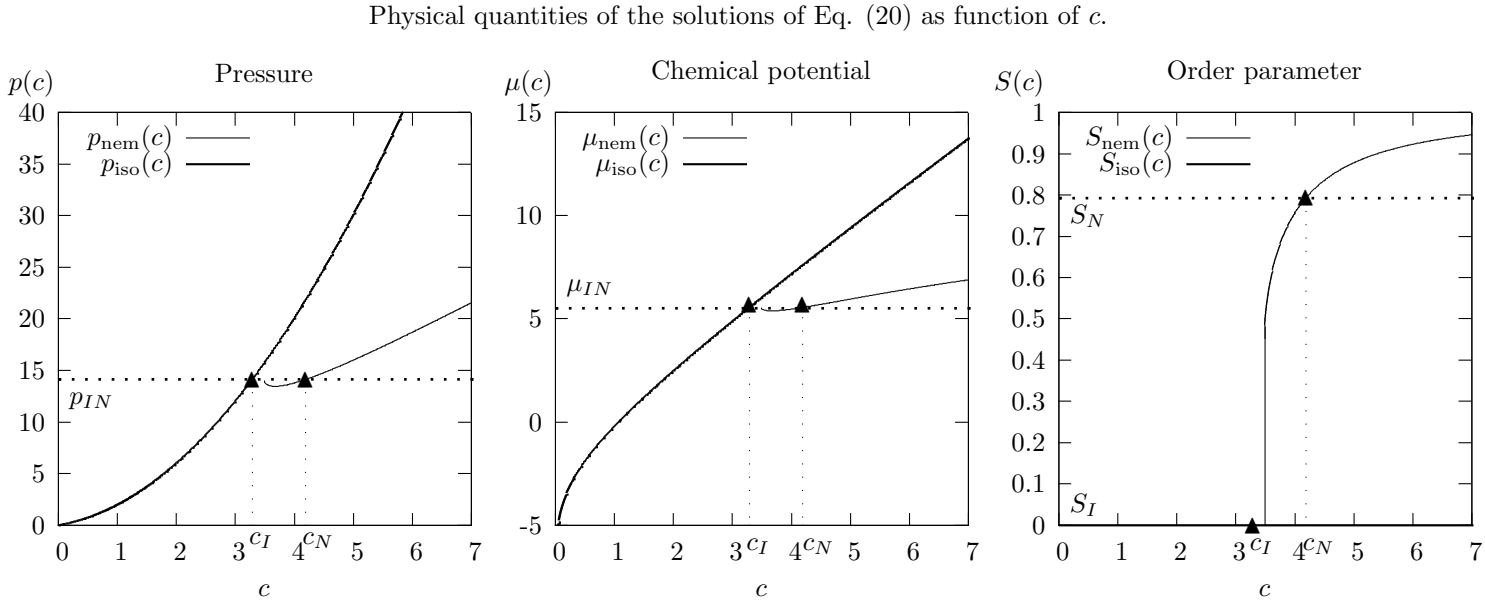

Figure 5: Graphs of the pressure, chemical potential and order parameter respectively for the isotropic and nematic phases, with the coexistence values highlighted.

3 Binary Mixtures

Onsager theory can easily be extended for mixtures of different particles. The orientational free energy is replaced by a sum of the orientational free energy of each species; the excess free energy, which consist of the interactions between particles, now has separate terms for every pair of species; and an extra mixing free energy term is added, which favours the system to spread the particles of different species evenly.

Lekkerkerker et al. argued in 1984 [7] that the same isotropic-nematic demixing happens in a binary mixture of long and short hard rods, but with different concentrations of the longer rods in the nematic phase compared to the isotropic phase. This is because when the thick rods are in the nematic phase and thus are aligned, there is little room for the shorter rods to point in every orientation with equal probability. It costs less energy to split the system in a nematic phase, where the longer rods are aligned and thus are efficient with the volume, and an isotropic phase, where the shorter rods can freely explore all orientations without being constricted by the aligned longer rods.

It was not until 1993 that Vroege and Lekkerkerker [8] argued that there should also appear a nematic-nematic demixing when the longer rods are three times larger than the shorter rods. This is similar to the isotropic-nematic demixing for binary mixtures, where the shorter rods are less aligned (but are still in a nematic phase) than the longer rods. In 1995, Sear and Jackson [9] showed that a mixture of hard rods can also have an isotropic-isotropic demixing. They showed it for a system of thick and thin hard rods, where the thicker rods are more than five times thicker than the thin rods. It has been argued that this demixing is due to the depletion effect, where the excluded volume per particle around the thick rods where thin rods can appear is smaller if the thicker rods have overlapping excluded volumes, thus favouring a thick rod rich phase and a thin rod rich phase.

It is also possible to extend Onsager theory to include charged rods [10] and chiral particles [11].

3.1 Extension to Onsager theory

Next we consider a system with N_σ hard rods of species $\sigma = 1, 2$ with diameters D_σ and identical length L in a macroscopic volume V, and define the diameter ratio $d = D_2/D_1 > 1$. We characterize the thermodynamic state by the dimensionless number density $c = (N_1 + N_2)B_2/V$ with respect to the second virial coefficient of the thinner rods in the isotropic phase $B_2 = (\pi/4)L^2D_1$; and the composition variable $x = N_2/(N_1 + N_2)$, which is the mole fraction of the thick rods. We also consider separate ODFs $\psi_\sigma(\theta)$ for the two different species, such that $\psi(\theta) = (1-x)\psi_1(\theta) + x\psi_2(\theta)$. Filling in this substitution, the orientational term of Eq. (19) becomes

$$\begin{aligned}
&4\pi \int_0^{\pi/2} \mathrm{d}\theta \sin\theta \psi(\theta) \log(\psi(\theta)) \\
&= 4\pi \int_0^{\pi/2} \mathrm{d}\theta \sin\theta \left((1-x)\psi_1(\theta) + x\psi_2(\theta)\right) \log((1-x)\psi_1(\theta) + x\psi_2(\theta)) \\
&= 4\pi \Big((1-x)\log(1-x) \int_0^{\pi/2} \mathrm{d}\theta \sin\theta \psi_1(\theta) + x \log x \int_0^{\pi/2} \mathrm{d}\theta \sin\theta \psi_2(\theta) \\
&+ \int_0^{\pi/2} \mathrm{d}\theta \sin\theta \left((1-x)\psi_1(\theta)\log(\psi_1(\theta)) + x\psi_2(\theta)\log(\psi_2(\theta))\right) \Big) \\
&= f_{\mathrm{mix}}(x) + (1-x) f_{\mathrm{or},1} + x f_{\mathrm{or},2}
\end{aligned} \tag{37}$$

where $f_{\mathrm{or},\sigma}$ is the orientational term of the free energy of the monodisperse system of species σ, replacing ψ with ψ_σ:

$$\begin{aligned}
f_{\mathrm{or}}(x) &= (1-x) f_{\mathrm{or},1} + x f_{\mathrm{or},2} \\
&= 4\pi \int_0^{\pi/2} \mathrm{d}\theta \sin\theta \left((1-x)\psi_1(\theta)\log(\psi_1(\theta)) + x\psi_2(\theta)\log(\psi_2(\theta))\right)
\end{aligned} \tag{38}$$

Using the identity $4\pi \int_0^{\pi/2} \mathrm{d}\theta \sin\theta \psi_\sigma(\theta) = 1$, we can write the mixing term of the free energy as

$$f_{\mathrm{mix}}(x) = (1-x)\log(1-x) + x \log x. \tag{39}$$

The excess term f_{ex} of Eq. (19) is replaced in the same way. However, we have to take notice that the virial coefficients of the two species are not equal, from Eq. (11) is $B_{2,\mathrm{INL},\sigma} = 2L^2 D_\sigma |\sin\gamma|$. However, $B_{2,\mathrm{INL},2} = B_{2,\mathrm{INL},1} d$, thus the excess term of the free energy for a binary mixture is equal to

$$\begin{aligned} f_{\mathrm{ex}}(c,x,d) &= 32c \int_0^{\pi/2} \mathrm{d}\theta \int_0^{\pi/2} \mathrm{d}\theta' \sin\theta \sin\theta' K(\theta,\theta') \\ &\times \left((1-x)^2 \psi_1(\theta)\psi_1(\theta') + x(1-x)(1+d)\psi_1(\theta)\psi_2(\theta') + x^2 d\psi_2(\theta)\psi_2(\theta') \right), \end{aligned} \tag{40}$$

so the total free energy of the binary mixture is

$$f(c,x,d) = \log(c) + f_{\mathrm{mix}}(x) + f_{\mathrm{or}}(x) + f_{\mathrm{ex}}(c,x) \tag{41}$$

where f_{mix}, f_{or} and f_{ex} are defined in Eqs. (38)-(40).

Using the Euler-Lagrange equations, we can minimize f with respect to the ODFs by solving $\delta f / \delta \psi_\sigma(\theta) = 0$, which gives

$$\begin{aligned} \mu_1 &= \log\psi_1(\theta) + \frac{8c}{\pi} \int_0^{\pi/2} \mathrm{d}\theta' \sin\theta' K(\theta,\theta') \left(2(1-x)\psi_1(\theta') + x(1+d)\psi_2(\theta') \right), \\ \mu_2 &= \log\psi_2(\theta) + \frac{8c}{\pi} \int_0^{\pi/2} \mathrm{d}\theta' \sin\theta' K(\theta,\theta') \left((1-x)(1+d)\psi_1(\theta') + 2xd\psi_2(\theta') \right), \end{aligned} \tag{42}$$

where we fix both Lagrange multipliers μ_σ by normalizing the ODFs: $4\pi \int_0^{\pi/2} \mathrm{d}\theta \sin\theta \psi_\sigma(\theta) = 1$. Again it is easy to show that $\psi_{\mathrm{iso},\sigma}(\theta) = 1/(4\pi)$ are solutions to Eq. (42).

Once a solution for (42) has been found, one can calculate f by plugging in the resulting ODFs in (41). By knowing f, one can calculate multiple physical quantities related to the system. The physical quantities we are interested in are the pressure p, chemical potentials μ_1 and μ_2, the order parameters S_σ and the Gibbs free energy G. It is convenient to look at the dimensionless pressure $\beta p B_2$, dimensionless chemical potentials $\beta\mu_1$ and $\beta\mu_2$, and the Gibbs free energy per particle per $k_B T$ g, which are defined as

$$p \equiv \beta\hat{p}B_2 = \left(\frac{B_2 \beta \partial F}{\partial V} \right)_{N_1,N_2} = \left(\frac{\partial f}{\partial c} \right)_x c^2, \tag{43}$$

$$\mu_1 \equiv \beta\hat{\mu}_1 = \left(\frac{\beta\partial F}{\partial N_1} \right)_{V,N_2} = f - \left(\frac{\partial f}{\partial x} \right)_c x + \left(\frac{\partial f}{\partial c} \right)_x c, \tag{44}$$

$$\mu_2 \equiv \beta\hat{\mu}_2 = \left(\frac{\beta\partial F}{\partial N_2} \right)_{V,N_2} = f + \left(\frac{\partial f}{\partial x} \right)_c (1-x) + \left(\frac{\partial f}{\partial c} \right)_x c. \tag{45}$$

$$S_\sigma = 4\pi \int_0^{\pi/2} \mathrm{d}\theta \sin\theta \psi_\sigma(\theta) \frac{3\cos^2\theta - 1}{2} \tag{46}$$

$$\mathrm{d}G = -S\,\mathrm{d}T + V\,\mathrm{d}p + \mu_1\,\mathrm{d}N_1 + \mu_2\,\mathrm{d}N_2 \tag{47}$$

$$g = \frac{F + pV}{N k_B T} = f + \frac{\beta p B_2}{c} \tag{48}$$

Starting from here, p and μ_σ refer to the dimensionless versions of the pressure and chemical potentials respectively.

3.2 High pressure limit

To study the nematic-nematic coexistence, we have to look at large concentrations c, and thus large pressures p. However, the resulting ODFs from Eq. (42) are extremely peaked around $\theta = 0$, causing even very fine θ-grids to be too crude for accurate results. It is more efficient to scale the ODFs with respect to the concentration c, and then expand the free energy f for large c [14] [15].

First we introduce the reduced ODFs

$$\phi_\sigma(\theta) = \frac{\psi_\sigma(\theta)}{\psi_\sigma(0)} \tag{49}$$

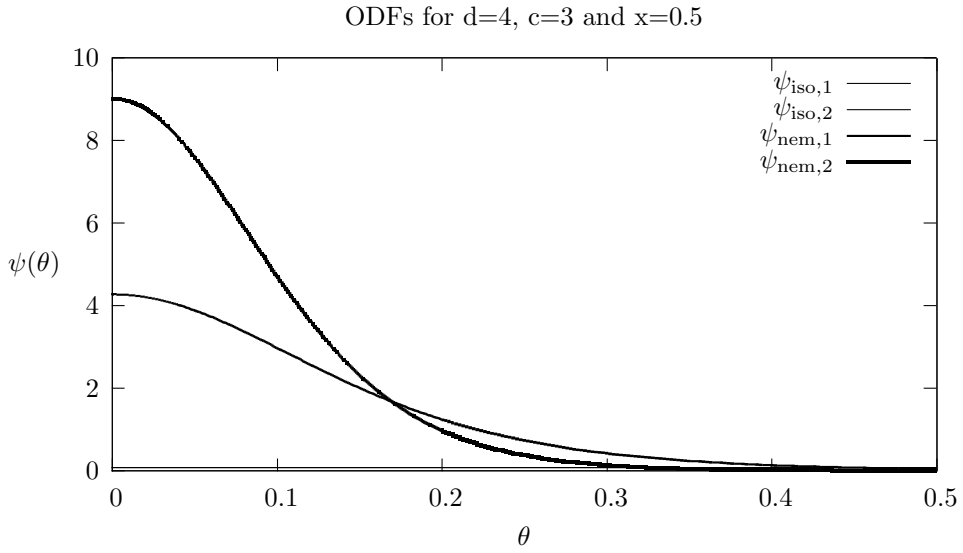

Figure 6: Solutions of the equations in (42) for diameter ratio $d = 4$, dimensionless number density $c = 3$ and composition variable $x = 0.5$. $\psi_{\mathrm{iso},\sigma} = 1/(4\pi)$ are the solutions of the isotropic phase, and $\psi_{\mathrm{nem},\sigma}$ are the solutions of the nematic phase. It shows that in the nematic case the thicker rods are more alligned to the nematic director than the thinner rods. The ODFs for different parameters yield similar shapes of the nematic solutions, but with different width and heights.

which is equal to 1 at $\theta = 0$ by construction. Next we introduced the scaled polar angle $t = c\theta$. Using this definition, we can expand the terms in (41) for large c:

$$\begin{aligned} K(\theta,\theta') &= cK_0(t,t') + K_2(t,t')/c + \mathcal{O}(1/c^3), \\ \mathrm{d}\theta \sin\theta &= (\mathrm{d}tt)/c^2 \times (1 - t^2/6c^2 + \mathcal{O}(1/c^4)), \\ \phi_\sigma(\theta) &= \phi_{\sigma 0}(t) + \phi_{\sigma 1}(t)/c + \phi_{\sigma 2}(t)/c^2 + \mathcal{O}(1/c^3). \end{aligned} \tag{50}$$

where the kernels K_0 and K_2 are equal to

$$\begin{aligned} K_0(t,t') &= 4(t+t')E\left(\frac{4tt'}{(t+t')^2}\right) \\ K_2(t,t') &= \frac{1}{3}(t+t')\left((t-t')^2 K\left(\frac{4tt'}{(t+t')^2}\right) - 3(t^2+t'^2)E\left(\frac{4tt'}{(t+t')^2}\right)\right) \end{aligned} \tag{51}$$

where $K(x)$ and $E(x)$ are the elliptic integrals of the first and second kind, respectively. Note that K_n for odd n are equal to 0.

Substituting these expansions in Eq. (42), and using the short-hand notations $\Delta K_n(t,t') = K_n(t,t') - K_n(0,t')$ and $\Xi_{\sigma\rho} = \int \mathrm{d}tt\phi_{\sigma\rho}(t)$, we get

$$\begin{aligned} \log\phi_{1,0}(t) &= -\frac{2}{\pi^2}\int_0^{\pi c/2} \mathrm{d}t't'\Delta K_0(t,t')\left(2(1-x)\frac{\phi_{10}(t')}{\Xi_{10}} + x(1+d)\frac{\phi_{20}(t')}{\Xi_{20}}\right), \\ \log\phi_{1,0}(t) &= -\frac{2}{\pi^2}\int_0^{\pi c/2} \mathrm{d}t't'\Delta K_0(t,t')\left((1-x)(1+d)\frac{\phi_{10}(t')}{\Xi_{10}} + 2xd\frac{\phi_{20}(t')}{\Xi_{20}}\right) \end{aligned} \tag{52}$$

$$
\begin{aligned}
\phi_{11}(t) &= -\frac{2}{\pi^2}\phi_{10}(t)\int_0^{\pi c/2}\mathrm{d}t't'\Delta K_0(t,t') \\
&\quad\times\left(2(1-x)\left(\frac{\phi_{11}(t')}{\Xi_{10}}-\frac{\phi_{10}(t')\Xi_{11}}{\Xi_{10}^2}\right)+x(1+d)\left(\frac{\phi_{21}(t')}{\Xi_{20}}-\frac{\phi_{20}(t')\Xi_{21}}{\Xi_{20}^2}\right)\right), \\
\phi_{21}(t) &= -\frac{2}{\pi^2}\phi_{20}(t)\int_0^{\pi c/2}\mathrm{d}t't'\Delta K_0(t,t') \\
&\quad\times\left((1-x)(1+d)\left(\frac{\phi_{11}(t')}{\Xi_{10}}-\frac{\phi_{10}(t')\Xi_{11}}{\Xi_{10}^2}\right)+2xd\left(\frac{\phi_{21}(t')}{\Xi_{20}}-\frac{\phi_{20}(t')\Xi_{21}}{\Xi_{20}^2}\right)\right),
\end{aligned}
\tag{53}
$$

$$
\begin{aligned}
\phi_{12}(t) &= -\frac{2}{\pi^2}\phi_{10}(t)\left(2(1-x)v_1(t)+x(1+d)v_2(t)\right)+\frac{\phi_{11}^2(t)}{2\phi_{10}^2(t)}, \\
\phi_{22}(t) &= -\frac{2}{\pi^2}\phi_{20}(t)\left((1-x)(1+d)v_1(t)+2xdv_2(t)\right)+\frac{\phi_{21}^2(t)}{2\phi_{20}^2(t)},
\end{aligned}
\tag{54}
$$

with

$$
\begin{aligned}
v_\sigma(t) = \frac{1}{\Xi_{\sigma0}}\int_0^{\pi c/2}\mathrm{d}t't'\Big(&-\frac{t'^2}{6}\Delta K_0(t,t')\phi_{\sigma0}(t')+\Delta K_2(t,t')\phi_{\sigma0}(t')+\Delta K_0(t,t')\phi_{\sigma2}(t') \\
&+\Delta K_0(t,t')\phi_{\sigma1}\frac{\Xi_{\sigma1}}{\Xi_{\sigma0}}+\Delta K_0(t,t')\phi_{\sigma0}(t')\frac{\Xi_{\sigma1}^2-\Xi_{\sigma0}\int\mathrm{d}t''t''(\phi_{\sigma2}(t'')-\frac{t''^2}{6})}{\Xi_{\sigma0}^2}\Big).
\end{aligned}
\tag{55}
$$

Note however that the equations in (53) are linear integral equations with respect to $\phi_{\sigma1}$ without a source term, and thus are equal to 0. Therefore we can remove Eq. (53) and simplify (55) by

$$
\begin{aligned}
v_\sigma(t) = \frac{1}{\Xi_{\sigma0}}\int_0^{\pi c/2}\mathrm{d}t't'\Big(&-\frac{t'^2}{6}\Delta K_0(t,t')\phi_{\sigma0}(t')+\Delta K_2(t,t')\phi_{\sigma0}(t') \\
&+\Delta K_0(t,t')\phi_{\sigma2}(t')-\Delta K_0(t,t')\phi_{\sigma0}(t')\frac{\int\mathrm{d}t''t''(\phi_{\sigma2}(t'')-\frac{t''^2}{6})}{\Xi_{\sigma0}}\Big).
\end{aligned}
\tag{56}
$$

The $\phi_{\sigma\rho}$ terms still are dependent on c: they appear in the integration limits. However, the ODFs decay exponentially to 0 (see Fig. 7). For any integrable function $h(t)$ the following holds:

$$
\int_0^{\pi c/2}\mathrm{d}th(t)=\int_0^{\infty}\mathrm{d}th(t)-\int_{\pi c/2}^{\infty}\mathrm{d}th(t). \tag{57}
$$

If $h(t)$ is an exponentially decaying function $h(t)\sim\exp(-\lambda t)$, then the last term of Eq. (57) is equal to

$$
\int_{\pi c/2}^{\infty}\mathrm{d}th(t)\sim\frac{1}{\lambda}\exp(-\lambda\pi c/2)\xrightarrow{c\to\infty}0. \tag{58}
$$

Thus we can replace $\int_0^{\pi c/2}$ with $\int_0^{\infty}$ in Eqs. (52)-(56), meaning these equations are independent of c.

Using this expansion, we can expand the free energy too

$$
f(c,x)=3\log c+f_0(x)+f_2(x)/c^2+\mathcal{O}(1/c^4). \tag{59}
$$

We will not show the derivation of f_0 and f_2 explicitly, because the calculations are long but straightforward.

After calculating $f(c,x)$, we can calculate the physical quantities in the same way as Eqs. (43)-(45) using Eq. (59)

$$
p=\frac{\partial f}{\partial c}c^2=3c-\frac{2}{c}f_2(x) \tag{60}
$$

$$
\mu_1=f-\frac{\partial f}{\partial x}x+\frac{\partial f}{\partial c}c=3\log c+f_0(x)-xf_0'(x)+3-\frac{1}{c^2}\left(f_2(x)-xf_2'(x)\right) \tag{61}
$$

$$
\mu_2=f+\frac{\partial f}{\partial x}(1-x)+\frac{\partial f}{\partial c}c=3\log c+f_0(x)+(1-x)f_0'(x)+3-\frac{1}{c^2}\left(f_2(x)+(1-x)f_2'(x)\right) \tag{62}
$$

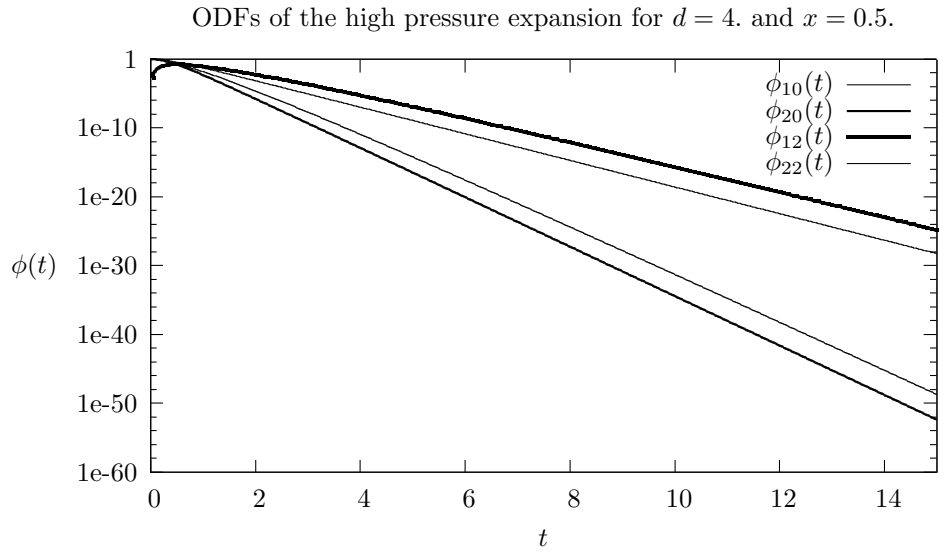

Figure 7: Logarithmic plot of the solutions of Eqs. (52) and (54), showing the exponential decay required to perform the limit in Eq. (58).

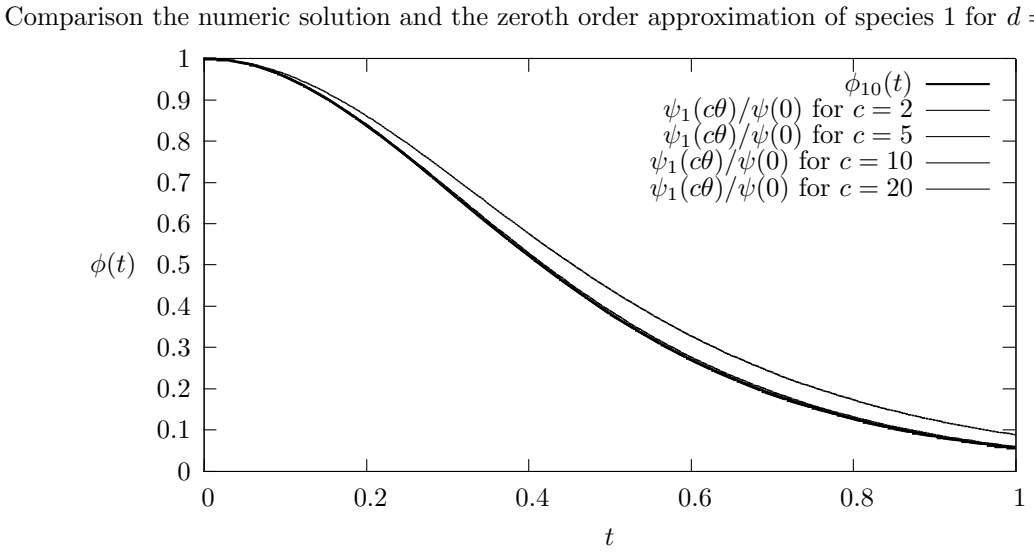

Figure 8: Comparison between the zeroth order term of the high pressure expansion, which is the solution of Eq. (53); and the solution of Eq. (20), for species 1. For $c = 2$, there is large difference between the zeroth order approximation and the numerical solution, because the next order in the expansion scales with $1/2^2 = 1/4$. For $c = 5$, the two curves lie much closer, since the next order in the expansion scales with $1/5^2 = 1/25$.

Gibbs free energy of the isotropic phase for $d = 10$ and $p = 2$, with its common tangent.

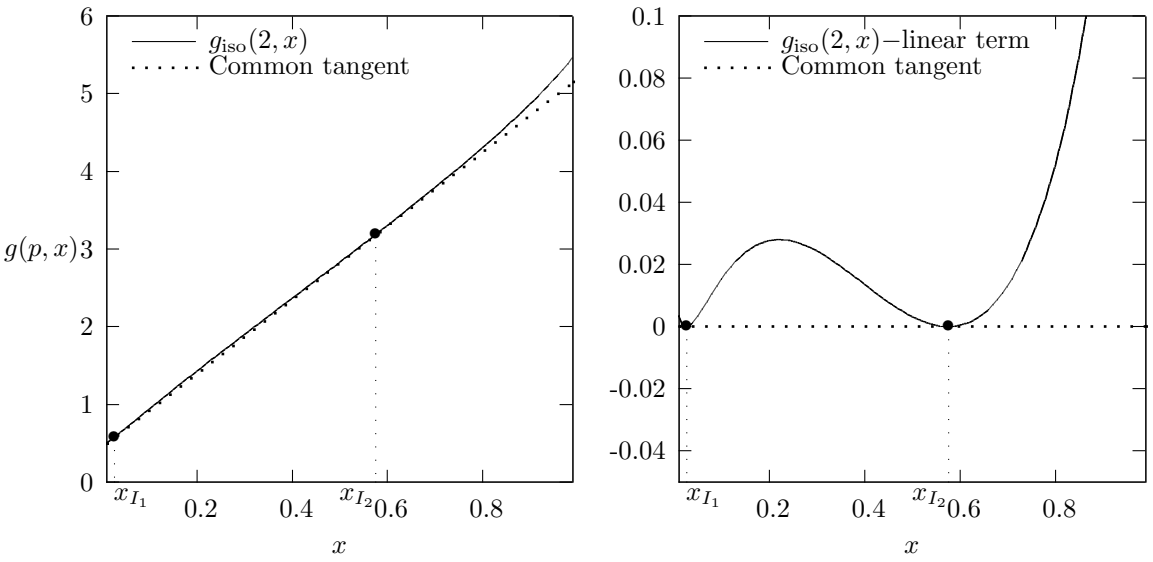

Figure 9: On the left: $g(p = 2, x)$, which is in the isotropic phase, and its common tangent with itself. Because the common tangent is hard to see, we subtract in the figure right a linear term. The common tangent touches $g(p, x)$ at the points $x_{I_1} \simeq 0.0257$ and $x_{I_2} \simeq 0.576$, thus the volume splits into two subvolumes with isotropic phases with compositions x_{I_1} and x_{I_2}.

where $f_n'(x) = \mathrm{d}f_n(x)/\,\mathrm{d}x$.

3.3 Phase coexistence

Once we have solved Eq. (42) and calculated the related physical quantities (43)-(46) for fixed d and variable c and x, we can compare the (Gibbs) free energy for both the isotropic and the nematic solutions. The isotropic phase is more energetic favourable for $x \lesssim 0.568$ while the nematic phase is favoured for $x \gtrsim 0.568$. However, an even more energetic favourable state is by phase seperating the isotropic from the nematic part. Such a phase coexistence can only happen if we find two solutions of Eq. (42) where the chemical potentials and pressures are the same:

$$\mu_1(c_1, x_1) = \mu_1(c_2, x_2), \quad \mu_2(c_1, x_1) = \mu_2(c_2, x_2), \quad p(c_1, x_1) = p(c_2, x_2) \tag{63}$$

where p and μ_σ are defined in Eqs. (43) - (45). Note that these are 3 equations with 4 unknowns, so we add a fourth equation fixing the pressure: $p(c_1, x_1) = p$. This equation is equal to finding the common tangent between the Gibbs free energies of the isotropic and the nematic phase, as demonstrated in Fig. 9.

Isotropic-nematic phase coexistence is not the only type of coexistence found in binary systems of thin and thick hard rods: for high pressure ($p \gtrsim 14$) and high diameter ratios ($d \gtrsim 4$), a nematic-nematic phase coexistence is energetic favourable, where one nematic system has significantly more colloids of species 1. For even greater diameter ratios ($d \gtrsim 8$) and low pressures ($p \lesssim 2.5$), an isotropic-isotropic phase coexistence appears.

Because the equations at (63) are three equations with four unknowns, a solution curve appears. By adding a fourth constraint fixing the pressure $p(c_1, x_1) = p$, we can visualize this solution space in a phase diagram. Phase diagrams in the p-x plane are shown in Fig. 10.

These phase diagrams can also be represented in different planes, for example in the $c_1 - c_2$ plane, where $c_1 = (1 - x)c$ and $c_2 = xc$ are the dimensionless number densities of species 1 and 2 respectively; or the $\mu_1 - \mu_2$ plane, which is of main interest in sedimentation profiles.

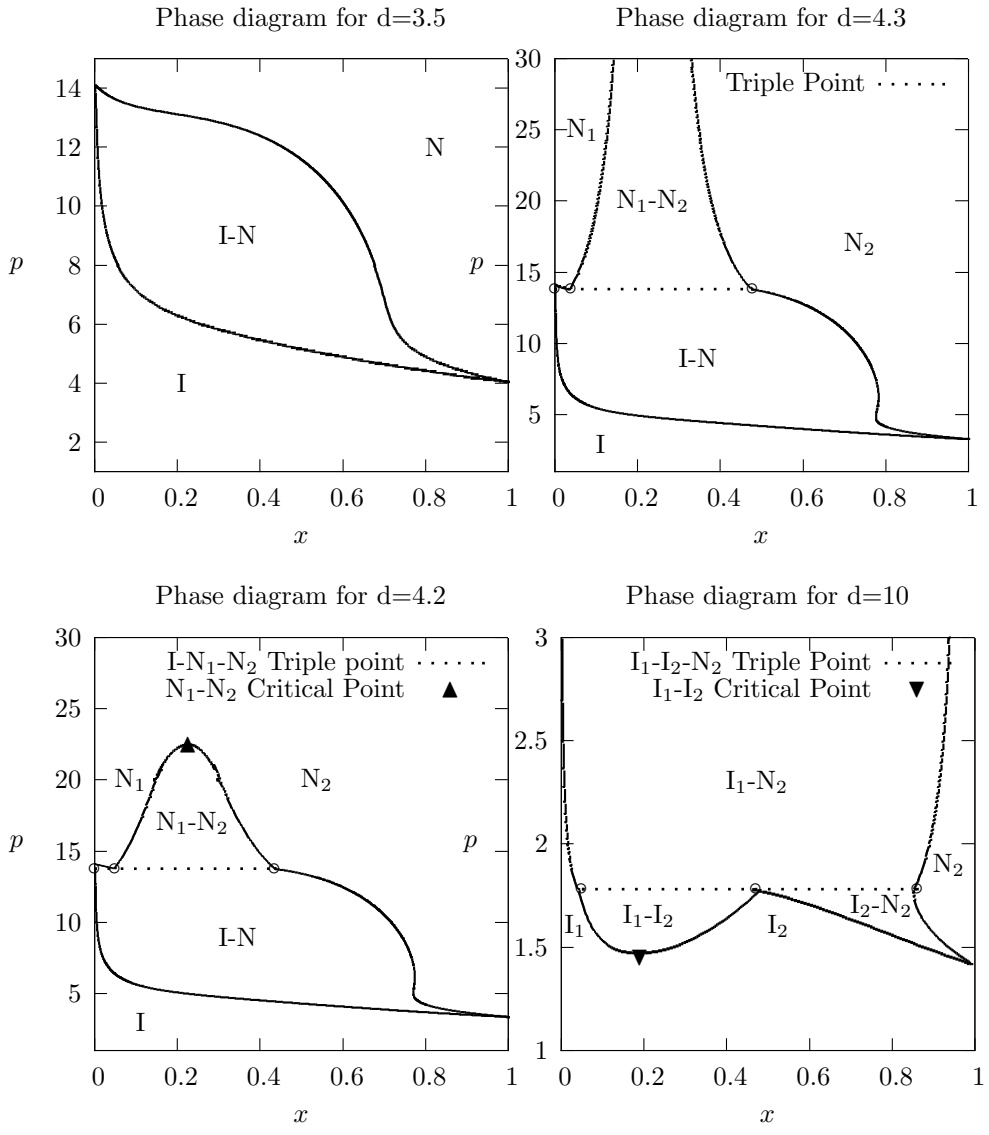

Figure 10: Phase diagrams in the p-x plane for $d = 3.5, 4.2, 4.3$ and 10.

Phase diagram in the $\mu_1 - \mu_2$ plane for diameter ratios $d = 3.5$ and $d = 10$.

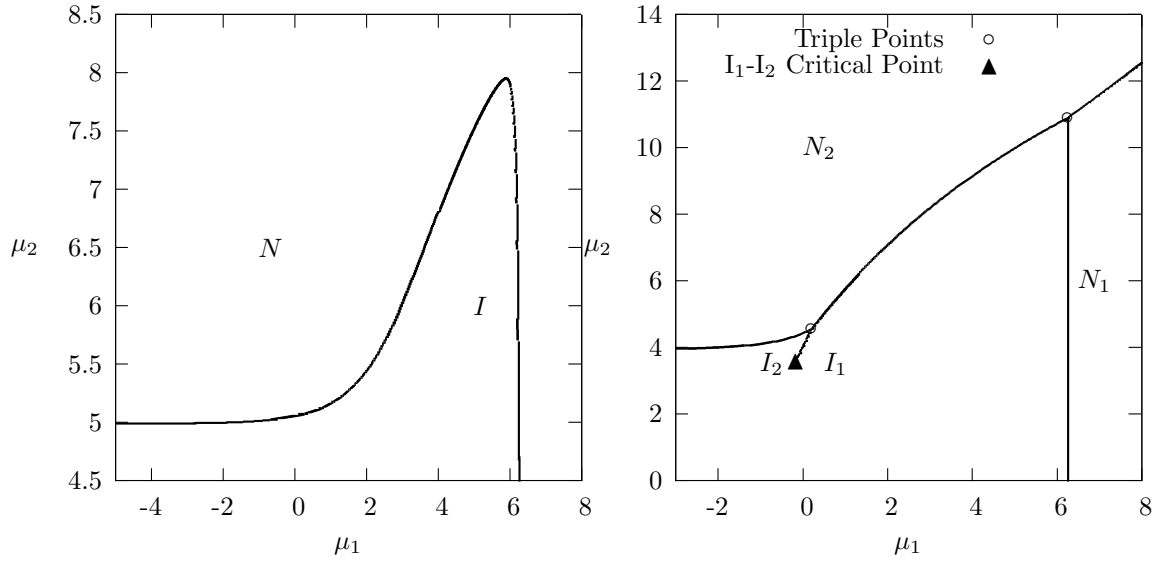

Figure 11: Phase diagrams in the μ_1 - μ_2 representation for diameter ratios $d = 3.5$ and $d = 10$ respectively, with the critical and triple points highlighted.

Phase diagram in the $c_1 - c_2$ plane for diameter ratios $d = 3.5$ and $d = 10$.

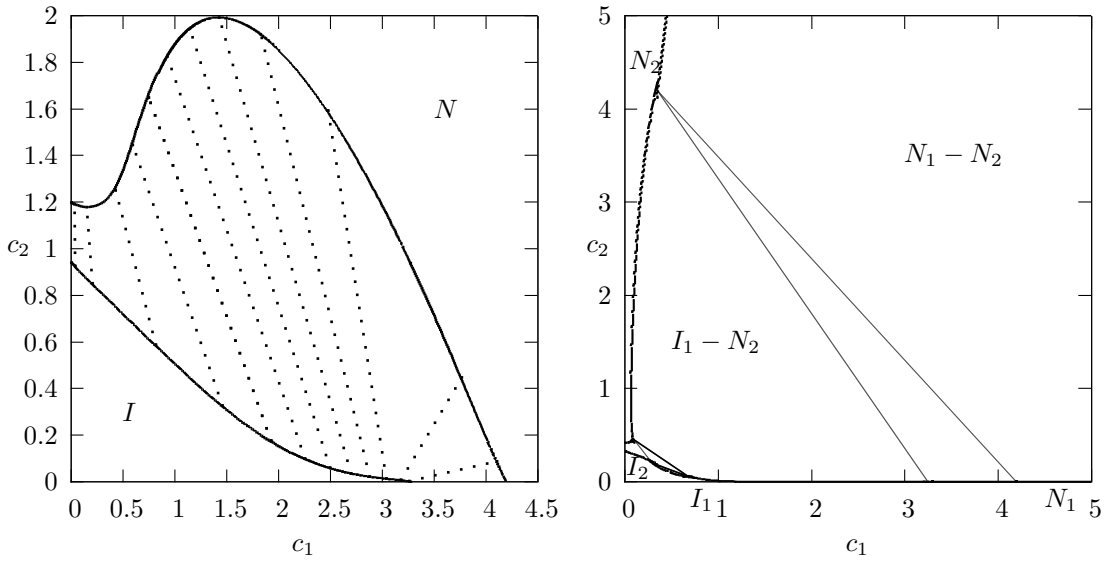

Figure 12: Phase diagrams in the c_1 - c_2 representation for diameter ratios $d = 3.5$ and $d = 10$ respectively. Coexistence are dotted in the picture on the left. All phase lines stop at the c_1 axis at the densities of the monodisperse system, while at the c_2 axis, these endpoints multiplied with a factor $1/d$. In the picture on the right, the triangles represent the triple points, with the $I_1 - I_2 - N_2$ triple point on the left, and the $I_1 - N_1 - N_2$ triple point on the right.

4 Sedimentation

Experimental research on binary mixtures is often more challenging than studying monodisperse systems because of the effects of gravity which are often unavoidable. By updating the free energy with height-dependent density profiles caused by gravity, one can calculate the grand chemical potential and minimize this to study the effects of gravity in binary mixtures. While this calculation is straightforward, many interesting phenomena happen when putting a binary mixture in a test tube. For example, an isotropic phase can appear between two nematic phases. Even for relatively simple systems with low diameter ratios, where there is no demixing except for the isotropic-nematic demixing, multiple layers of alternating isotropic and nematic phases appear. Another interesting phenomena is that the fraction of the heavier particles is not always decreasing higher in the tube, it is quite possible that a heavy particle rich layer appears between two phases dominated by lighter particles. [16] [17] The theory to model this behaviour is inspired by [18] [19].

The grand potential functional as function of the density is given by

$$\begin{aligned}\Omega[\rho_1(\vec{x},\theta),\rho_2(\vec{x},\theta)] &= \mathcal{F}[\rho_1(\vec{x},\theta),\rho_2(\vec{x},\theta)] \\ &+ \int \mathrm{d}^3\vec{x} \int \mathrm{d}\theta \sin\theta \Big(\rho_1(\vec{x},\theta)(V_{\mathrm{ext},1}(\vec{x},\theta)-\mu_1) + \rho_2(\vec{x},\theta)(V_{\mathrm{ext},2}(\vec{x},\theta)-\mu_2)\Big)\end{aligned} \tag{64}$$

where $\mathcal{F}[\rho_1,\rho_2]$ is the free energy functional and $V_{\mathrm{ext},\sigma}$ is an external potential on species σ. We can approximate the free energy functional using a local density approximation because the gravitational length of the particles, which is often in the order of a millimetre, is much larger than the size of the colloids, which is of the order of nanometres. Using this approximation, the free energy functional can be approximated as

$$\mathcal{F}[\rho(z,\theta)] \approx \int \mathrm{d}^3\vec{x} f_b(\rho_1(\vec{x}),\rho_2(\vec{x})) \tag{65}$$

where $f_b(\rho) = F_b(N,V,T)/(Vk_BT)$ is the bulk free energy per volume per k_BT, as defined in Eq. (41). Using gravity as our external potential $V_{\mathrm{ext},\sigma} = m_\sigma g z$, Eq. (64) reduces to

$$\Omega[\rho_1(z),\rho_2(z)] = A\int \mathrm{d}z \Big(f_b(\rho_1(z),\rho_2(z)) + \rho_1(z)(m_1gz-\mu_1) + \rho_2(z)(m_2gz-\mu_2)\Big), \tag{66}$$

where A is a macroscopic area perpendicular to z. We minimize this grand potential using the Euler-Lagrange equations

$$\begin{aligned}\frac{\delta\Omega[\rho_1(z),\rho_2(z)]}{\delta\rho_1(z)} = 0 = A\left(\frac{\partial f(\rho_1,\rho_2)}{\partial\rho_1} + m_1gz + \mu_1\right) = A(\mu_{1b}(\rho_1) + m_1gz - \mu_1) \\ \frac{\delta\Omega[\rho_1(z),\rho_2(z)]}{\delta\rho_2(z)} = 0 = A\left(\frac{\partial f(\rho_1,\rho_2)}{\partial\rho_2} + m_2gz + \mu_2\right) = A(\mu_{2b}(\rho_2) + m_2gz - \mu_2)\end{aligned} \tag{67}$$

and thus we want to solve the equations

$$\mu_{1b}(\rho_1(z),\rho_2(z)) = \mu_1 - m_1gz \qquad \mu_{2b}(\rho_1(z),\rho_2(z)) = \mu_2 - m_2gz \tag{68}$$

where $\mu_{\sigma b}$ is the bulk chemical potential and μ_σ is the chemical potential in absence of gravity. We can rewrite Eq. (68) as

$$\mu_{2b}(\mu_{1b}) = \frac{m_2}{m_1}(\mu_{1b}-\mu_1) + \mu_2 = s\mu_{1b} + a \tag{69}$$

with

$$s = m_2/m_1 \qquad\qquad a = \mu_2 - \mu_1 m_2/m_1 \tag{70}$$

the mass ratio between the two species and the scaled chemical potential difference respectively. Note that Eq. (69) is a linear equation with respect to μ_{1b}, and therefore are straight lines in the $\mu_1-\mu_2$ phase diagrams like those in Fig. 11.

These straight lines in the μ_1-μ_2 with slope s and point of crossing the μ_2-axis a correspond to the path the chemical potentials of the mixtures would take in a test tube with gravity. Each crossing with the phase-diagram corresponds to an interface between two phases, resulting in many different stacking sequences for varying s and a.

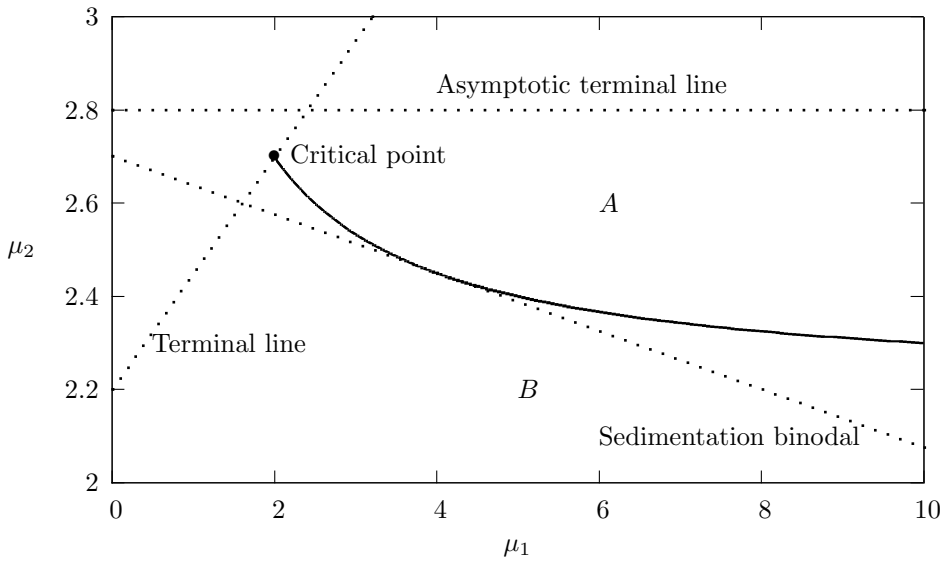

Figure 13: Example of a sedimentation binodal, terminal line and asymptotic terminal line for an example phase diagram between phases A and B. Sedimentation binodals are equal to the tangent lines of the phase diagram, terminal lines go through critical or triple points, and asymptotic terminal lines are parallel to the asymptote.

4.1 Phase stacking diagram

We can summarize all possible stacking sequences for different mass ratios s and scaled chemical potential differences a in a phase stacking diagram. By calculating when the straight line changes the amount of crossings with a line of the phase diagram in the $s - a$ parameter space, we can calculate the boundaries of different stacking sequences. There are three types of boundaries: sedimentation binodals, which correspond to the points in $s - a$ space where the line is tangent to a phase diagram line; terminal lines, which are lines that touch certain terminal points like critical and triple points; and asymptotic terminal lines, which appear due to the phase diagram having asymptotes. These boundaries are visualized in Fig. 13.

4.1.1 Sedimentation binodals

A straight line can cross a curve multiple times. When considering a one-dimensional curve $f(x)$ with an infinite domain $(-\infty, \infty)$, a variable straight line $a + sx$ where a and s vary changes its amount of intersections with $f(x)$ when it crosses a tangent of $f(x)$. By calculating these tangents and their corresponding a and s, we can draw a curve in the $s - a$ plane representing all tangent lines of $f(x)$. These curves in the $s - a$ plane correspond to a change in the amount of intersections the line $a + sx$ has with $f(x)$, and thus is the boundary between two different stacking sequences.

By calculating the curves $\mu_{1\alpha} : [\mu_{2,\alpha}, \mu_{2\alpha'}] \to I$ with $\mu_{1\alpha}(\mu_2)$, corresponding to the n lines in the $\mu_1 - \mu_2$ phase diagram like those in Fig. 11, we can parametrize the curve $b_\alpha(\mu_2) = (s(\mu_2), a(\mu_2))$ in the $s - a$ plane, which is equal to

$$b_{s,\alpha}(\mu_2) = \left(\frac{\mathrm{d}\mu_{1\alpha}}{\mathrm{d}\mu_2} \, , \, \mu_{1\alpha}(\mu_2) - \frac{\mathrm{d}\mu_{1\alpha}}{\mathrm{d}\mu_2} \mu_2 \right) \tag{71}$$

where μ_2 ranges from $[\mu_{2,\alpha}, \mu_{2\alpha'}]$. This results in n boundaries in the $s - a$ plane, with at one side a phase stacking $\ldots A \ldots$ and on the other side $\ldots ABA \ldots$, where A and B are the two phases of the $\mu_{1\alpha}(\mu_2)$ boundary in the $\mu_1 - \mu_2$ phase diagram, and $\ldots$ represent different phases due to other boundaries.

4.1.2 Terminal lines

When the curve $\mu_{1\alpha}(\mu_2)$ does not have an infinite domain, there is a terminal point $(\mu_{1\alpha}(\mu_{2\alpha}), \mu_{2\alpha})$ where the curve reaches a triple point (there curve splits into different lines $\mu_{1\beta}(\mu_2)$ and $\mu_{1\gamma}(\mu_2)$) or reaches a critical point, where the curve stops. Straight lines in the $\mu_1 - \mu_2$ plane change the amount of crossings with line α when crossing this terminal point. For a terminal point $(\mu_{1\alpha}, \mu_{2\alpha})$, all lines going through this point have the relation

$$b_{t,\alpha}(s) = (s\ ,\ \mu_{2\alpha} - \mu_{1\alpha} s) \tag{72}$$

where s ranges from $(-\infty, \infty)$. These are infinite straight lines in the $s-a$ plane. For a triple point, this is the boundary between phase stacking $\dots AB \dots$ and phase stacking $\dots ACB \dots$. For a critical point, this is the boundary between $\dots A \dots$ and $\dots A_1 A_2 \dots$, where A_1 and A_2 are phases which are able to continuous transform into each other via the supercritical phase A, without having to undergo a phase transition.

4.1.3 Asymptotic terminal lines

For very low concentrations c_σ of species σ, the chemical potential μ_σ goes to $-\infty$, while the other chemical potentials μ_γ with $\rho \neq \gamma$ go asymptotically to a certain value.

$$\lim_{\rho_\sigma \to 0} \mu_\sigma(\rho) = -\infty \qquad\qquad \lim_{\rho_\sigma \to 0} \mu_\gamma(\rho) = \mu_{\gamma,\mathrm{as}} \tag{73}$$

This is because at very low chemical potentials, the amount of particles of species σ N_σ goes lower, resulting in a very low ρ_σ. If species σ undergo a phase transition, the other particles γ will barely notice the change in structure of species σ due to the low amount of particles of species σ.

In the $s - a$ plane, lines parallel to the asymptote cross the asymptote if they have a slightly different slope s, thus a boundary between two phases in the phase stacking diagram is

$$b_{a,\alpha}(a) = (s, a) \tag{74}$$

where s is the slope of the asymptote, and a ranges from $(-\infty, \infty)$. These lines correspond to vertical lines at s in the $s - a$ plane. Asymptotic lines where $\mu_\sigma(\mu_2) \to finite$ if $\mu_2 \to \infty$ do not appear in the phase stacking diagram, because they correspond to lines with infinite slope $s = \infty$.

4.1.4 Results

Combining the results of Eq. (71), (72) and (74) in a single plot in the $s - a$ plane gives us the phase stacking diagram of this mixture. Diagrams for diameter ratios $d = 3.5$ and $d = 10$ are shown in Figs. (14) and (15) respectively.

4.2 Paths in other planes

For experimental purposes, the $\mu_1 - \mu_2$ plane is not a very interesting plane due to the difficulty of measuring the chemical potentials. However, it is possible to transform the straight lines in the chemical potentials plane to different planes.

4.2.1 Pressure-composition plane

The pressure-composition $(p - x)$ plane is an interesting plane to study because phase coexistences appear as horizontal lines, while giving information about the jump in composition along the coexistence surface. For a given diameter ratio d and mass ratio s, we can calculate the scaled chemical potential difference a using Eqs. (70), (44) and (45)

$$a(c, x) = \mu_2(c, x) - s\mu_1(c, x) = (1 - s)f + (1 - x - sx)\frac{\mathrm{d}f}{\mathrm{d}x} + (1 - s)c\frac{\mathrm{d}f}{\mathrm{d}c}. \tag{75}$$

With a coordinate transformation $c \to p(c, x)$ using Eq. (43), we can transform $a(c, x)$ to $a(p, x)$, and thus calculate for every point in the $p - x$ the corresponding point in the $\mu_1 - \mu_2$ plane, and since we have fixed s, the corresponding a associated with that point. Connecting

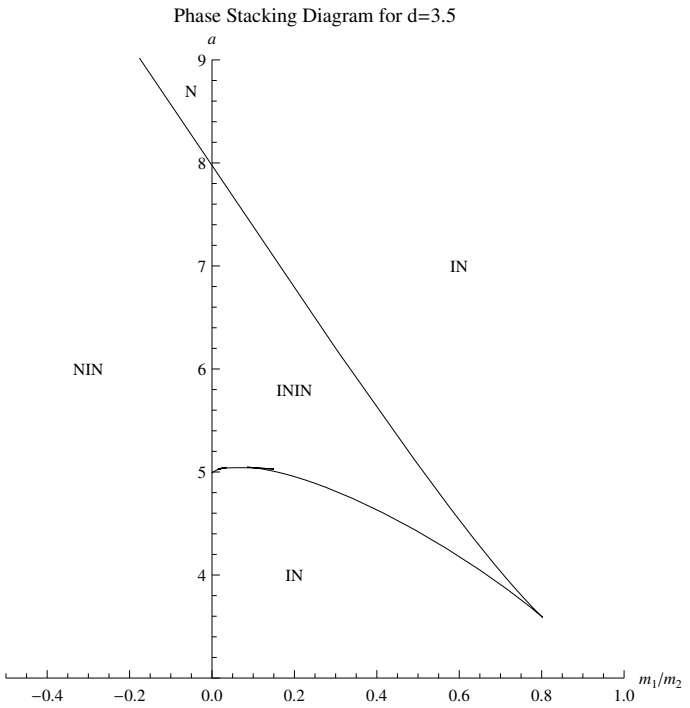

Figure 14: Phase stacking diagram for diameter ratio $d = 3.5$. This diagram consists of one sedimentation binodal and one asymptotic terminal line on the vertical line $s = m_1/m_2 = 0$.

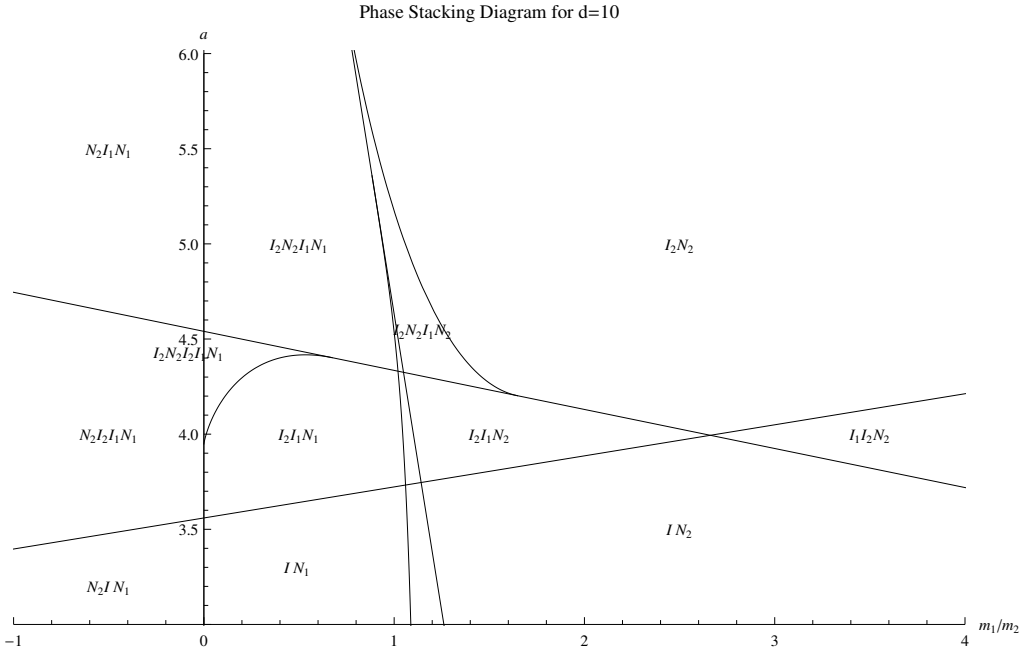

Figure 15: Phase stacking diagram for diameter ratio $d = 10$.. This diagram consists of five sedimentation binodals, one for each line segment in Fig. 11; three terminal lines, corresponding to the two triple points and one critical point; and one asymptotic terminal line related to the asymptote of the $I_2 - N_2$ line segment in the $\mu_1 - \mu_2$ representation. The three thin regions around $s = 1.1$ are from top to bottom: $I_2N_2I_1N_2N_1N_2$, $I_2I_1N_2N_1N_2$ and $IN_2N_1N_2$.

Phase stacking lines in the $p - x$ plane and $\mu_1 - \mu_2$ plane for $d = 3.5$ and $s = m_1/m_2 = 0.2$.

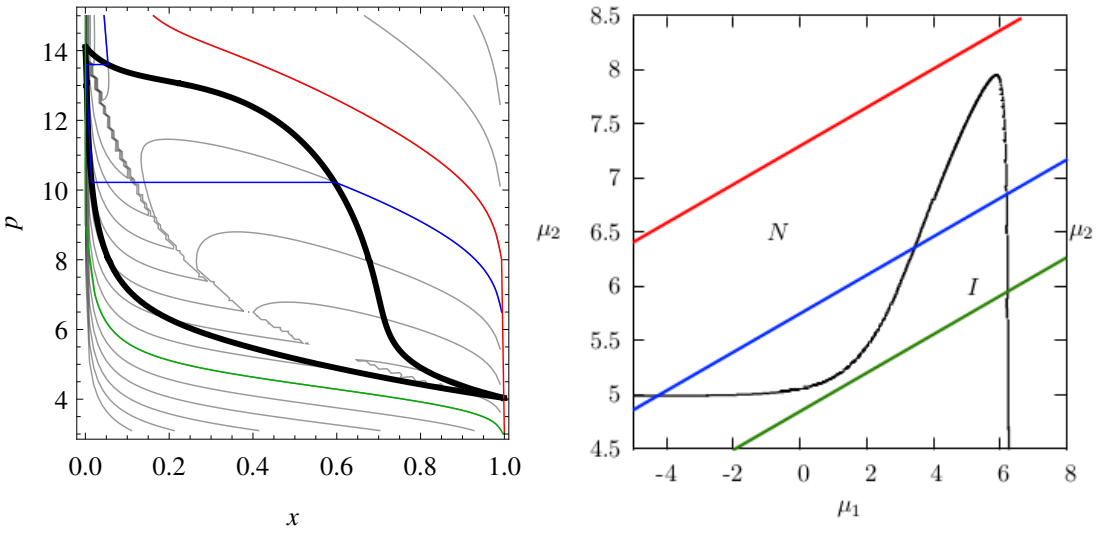

Figure 16: Phase stacking lines in the pressure-composition plane and the chemical potentials plane for diameter ratio $d = 3.5$ and mass ratio $m_1/m_2 = 0.2$. The thick black lines are the phase diagrams taken from Figs. 10 and 11 respectively. The thin lines correspond to lines of equal scaled chemical potential difference a, where we highlighted several of these lines with a colour. The coloured lines in the left picture are the same as those in the right picture, both showing that for example the blue line has a $I - N - I - N$ phase stacking.

the points with equal a gives us the curve the fluid obeys when in a tube with gravity. These curves are the think black lines in Figs. 16

When drawing the contours of a in the $p - x$ plane, we notice a discontinuity from the top left at $x = 0$ and $p = p_{crit}$, the monodisperse solution of thin rods, to the bottom right at $x = 1$ and $p = p_{crit}/d$, the monodisperse solution of the thick rods. This discontinuity corresponds to the points where the nematic phase is more favourable than the isotropic phase (but still less favourable than a coexistence of both phases), while the (Gibbs) free energy may be continuous at this line, other physical quantities do not have to be. This is illustrated in Fig. 5, where the chemical potential μ is discontinuous at the concentration c where the isotropic and nematic phases have equal free energy. Since a is dependent on the chemical potentials, we don't expect a to be continuous at this line in the $p - x$ plane.

When drawing the phase diagram on top of the contours of $a(p, x)$, the endpoints of the horizontal coexistence lines (p, x_1) and (p, x_2) have equal scaled chemical potential difference $a(p, x_1) = a(p, x_2)$. This is to be expected, since the horizontal coexistence lines in the $p - x$ plane correspond to a single point in the $\mu_1 - \mu_2$ phase diagram. For a isotropic-isotropic or nematic-nematic demixing, the contours of a associated with this demixing cross certain values of p multiple times. If there were no isotropic-isotropic or nematic-nematic demixing, the system would follow the a contour, and would have an interval with *decreasing* pressure when going down the tube, something non-physical.

4.2.2 Other chemical potential planes

Planes consisting of one of the chemical potentials are interesting because the difference in chemical potentials is equal (up to a constant) to the difference in height. Starting from Eq. (68), we can rewrite these equations as

$$\Delta\mu_\sigma = -m_\sigma g \Delta z \tag{76}$$

where $\Delta\mu_\sigma$ is the difference between two points on the same line $\mu_1(\mu_2) = a + s\mu_2$ and Δz the corresponding height difference. By introducing the gravitational length of species

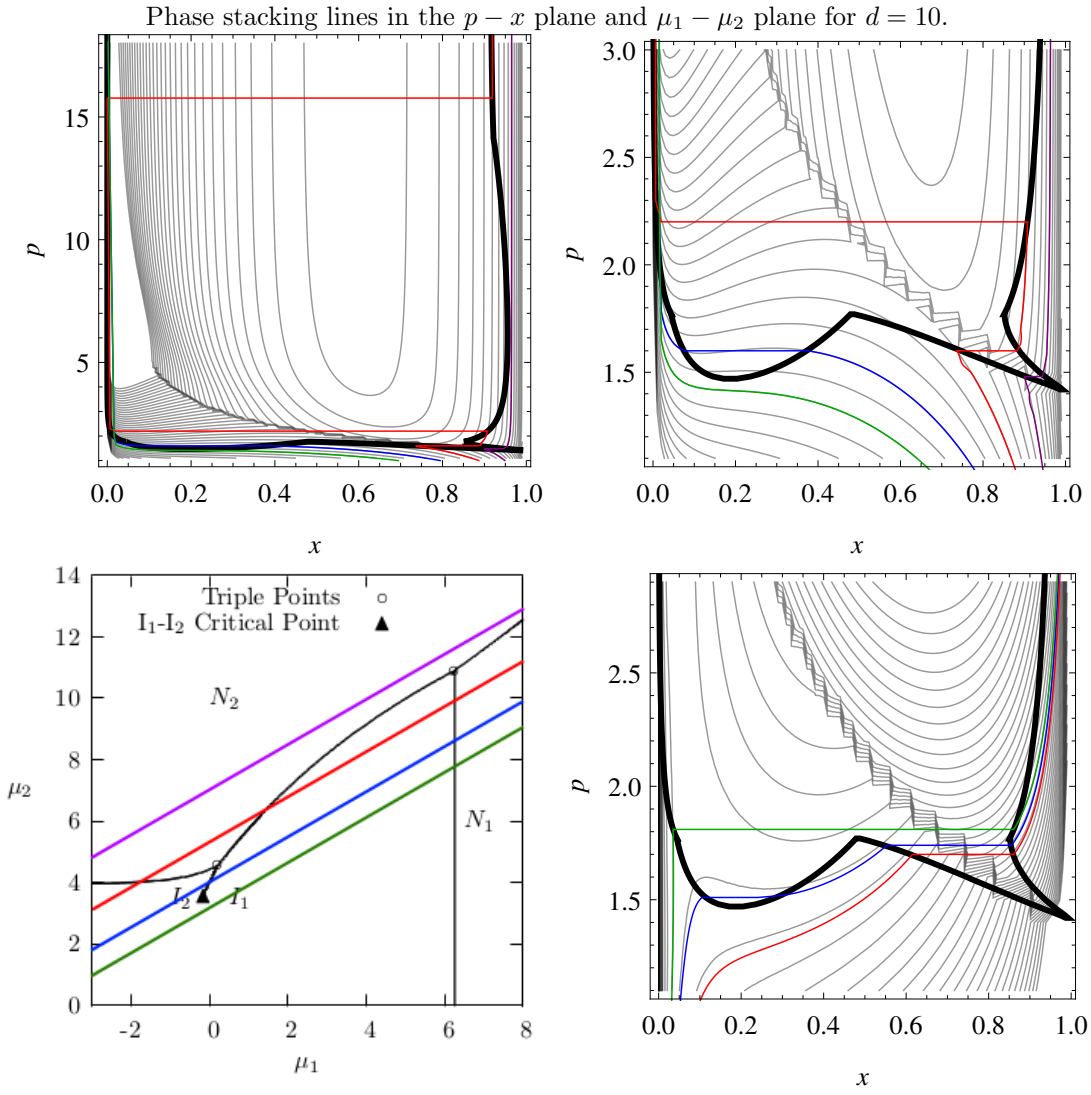

Figure 17: Phase stacking lines in the $p-x$ plane and the $\mu_1-\mu_2$ plane for diameter ratio $d=10$. All but the bottom right picture have mass ratio $s=1$, while the bottom right picture has mass ratio 3.5. The thick black lines are the phase diagrams taken from Figs. 10 and 11. The top right picture is the same as the top left pictures, but zoomed in at the low pressure regime. The thin lines correspond to lines of equal scaled chemical potential difference a, where we highlighted several of these lines with a colour. The coloured lines in the $s=1$ pictures are the same phase stacking, showing for example that the red line has phase stacking $I_2-N_1-I_1-N_2$.

Composition and order parameter as function of the height at $d = 10$ and $s = 1$.

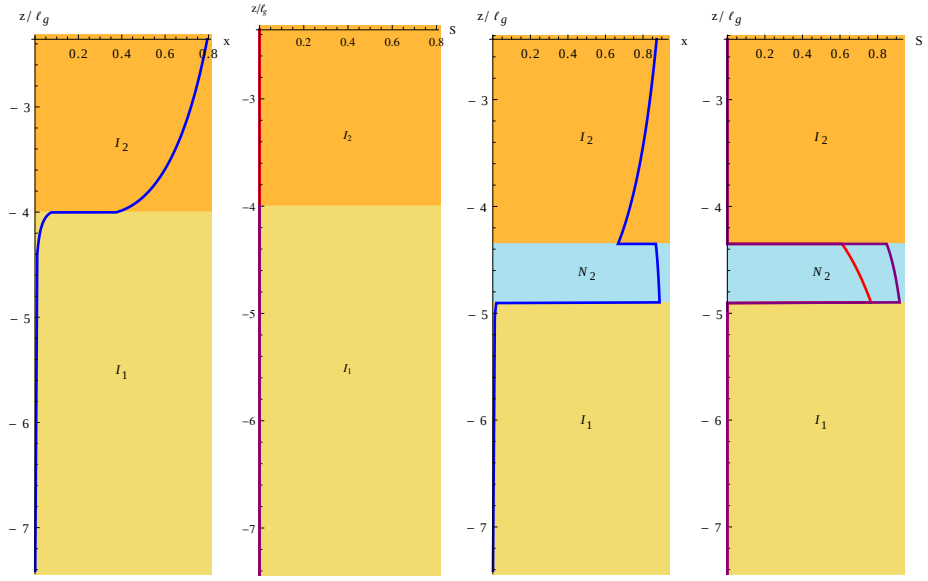

Figure 18: Composition x (blue) and order parameters S_1 (red) and S_2 (purple) as function of the height per gravitational length z/ℓ_g, with the different phases coloured. The two 'tubes' on the left are at $a = \mu_1 - s\mu_2 = 4.$, and the two tubes on the right for $a = 4.48$.

Composition and order parameter as function of the height at $d = 10$ and $s = 3.5$.

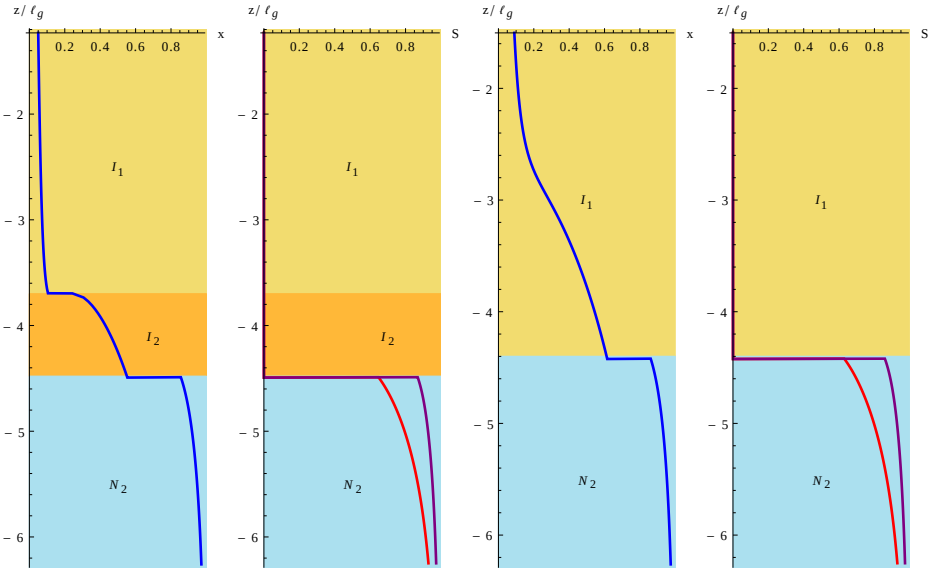

Figure 19: Composition x (blue) and order parameters S_1 (red) and S_2 (purple) as function of the height per gravitational length z/ℓ_g, with the different phases coloured. The two 'tubes' on the left are at $a = \mu_1 - s\mu_2 = 4.08$, and the two tubes on the right for $a = 4.42$.

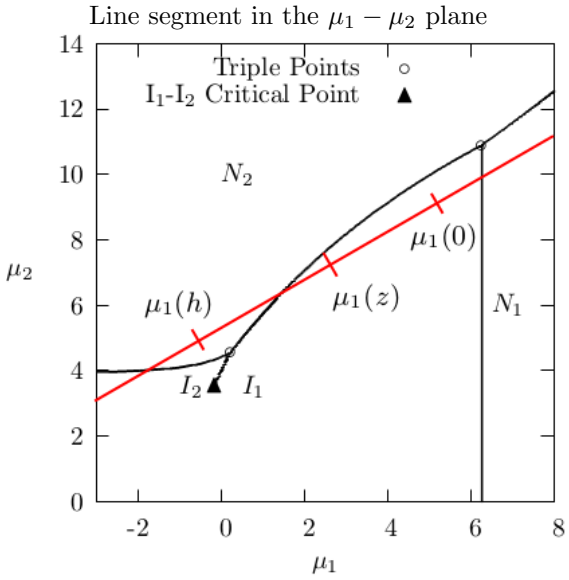

Figure 20: Line segment in the $\mu_1 - \mu_2$ plane. With a known diameter ratio d, mass ratio s, scaled chemical potential difference a and chemical potential of species 1 at height z $\mu_1(z)$, one can calculate the location of the line segment using Eqs. (69) and (78).

1 $\ell_g = k_B T/(m_1 g)$ we can relate the height difference to the non-dimensionless chemical potential difference

$$\Delta z = \ell_g \Delta\mu_1. \tag{77}$$

Thus, calculating the lines of equal scaled chemical potential a in a plane with both μ_1 and another physical quantity gives us this physical quantity as function of the height in a tube consisting of a mixture of these two species. In Figs. 18 and 19, the composition x and the order parameters S_1 and S_2 are shown as function of the height of such a finite tube.

4.3 Finite size effects

All these calculations assume the test tube has an infinite length in both direction, however, in Eq. (77) the chemical potential is proportional to the height in the test tube. Thus by measuring the chemical potential $\mu_1(z)$ at a certain height $z \in [0, h]$, where h is the height of the mixture in the test tube, the chemical potentials at the bottom and the top of the tube are

$$\mu_1(0) = \mu_1(z) - z/\ell_g, \qquad \mu_1(h) = \mu_1(z) + (h - z)/\ell_g. \tag{78}$$

This construction is visualized in Fig. 20. However, the chemical potential is difficult to measure. But by measuring the dimensionless number density c and composition x at a certain height z, one can calculate the chemical potential in Onsager theory using Eqs. (41), (42) and (44).

5 Thanks

This thesis could not be made without the help of certain people. First, I want to thank Prof. Dr. René van Roij for supervising this project and giving me countless tips and tricks on how to tackle this subject. Next I want to thank Tara Drwenski for helping and listening to me when I had any problems. I also want to thank Darius Keijdener for supporting me to get through the difficult parts of the thesis, as well as my family for supporting me all the time. There are many other people who supported me directly or indirectly during my thesis, and I would like to thank them as well.

References

[1] H. Zocher, Zeitschrift für anorganische und allgemeine Chemie **147**, 91 (1925)

[2] L. Onsager, Annals of the New York Academy of Sciences **51**, 627 (1949)

[3] J.D. Parsons, Physical Review A **19**, 1225 (1979)

[4] D. Frenkel, The Journal of Physical Chemistry **91**, 4912 (1987)

[5] D. Chandler, Introduction to Modern Statistical Mechanics (1987)

[6] R.H.H.G. van Roij, European Journal of Physics **26**, S57 (2005)

[7] H.N.W. Lekkerkerker, Ph. Coulon, R. van der Haegen and R. Deblieck, The Journal of Chemical Physics **80**, 3427 (1984)

[8] G.J. Vroege and H.N.W. Lekkerkerker, The Journal of Chemical Physics **97**, 3601 (1993)

[9] R.P. Sear and G. Jackson, The Journal of Chemical Physics **103**, 8684 (1995)

[10] E. Eggen, M. Dijkstra and R.H.H.G. van Roij, Physical Review E **79**, 041401 (2009)

[11] S. Belli, S. Dussi, M. Dijkstra and R.H.H.G. van Roij, Physical Review E **90**, 020503 (2014)

[12] R.H.H.G. van Roij, B. Mulder and M. Dijkstra, Physica A **261**, 374 (1998)

[13] R.H.H.G. van Roij and B. Mulder, Physical Review E **54**, 6430 (1996)

[14] R.H.H.G. van Roij and B. Mulder, The Journal of Chemical Physics **105**, 11237 (1996)

[15] R.H.H.G. van Roij and B. Mulder, Europhysics Letters **34**, 201 (1996)

[16] D. de las Heras, N. Doshi, T. Cosgrove, J. Phipps, D.I. Gittins, J.S. van Dijneveldt and M. Schmidt, Scientific Reports **2**, 789 (2012)

[17] K.R. Purdy, S. Varga, A. Galindo, G. Jackson and S. Fraden, Physical Review Letters **94**, 057801 (2005)

[18] D. de las Heras and M. Schmidt, Soft Matter **9**, 8636 (2013)

[19] D. de las Heras and M. Schmidt, Journal of Physics: Condensed Matter **27**, 194115 (2015)